Astron. Astrophys. 340, 351–370 (1998)

ASTRONOMY
AND
ASTROPHYSICS

NGC 3079: X-ray emission from the nuclear super-bubble and halo

W. Pietsch[1], **G. Trinchieri**[1,2], **and A. Vogler**[1]

[1] Max-Planck-Institut für Extraterrestrische Physik, Giessenbachstrasse, D-85740 Garching, Germany
[2] Osservatorio Astronomico di Brera, via Brera 28, Milano, Italy

Received 6 July 1998 / Accepted 2 October 1998

Abstract. We report the results of the spatial and spectral analysis of the ROSAT HRI and PSPC observations of the edge-on spiral galaxy NGC 3079. We detected several sources in the field of NGC 3079 with both PSPC and HRI, and complex emission from the inner 5′ around NGC 3079. We have identified possible counterparts for several of the sources outside NGC 3079 by comparison with optical plates and catalogues.

The X-ray emission from NGC 3079 has a $L_X = 3 \times 10^{40}$ erg s^{-1} and can be resolved into the following three components:

– Extended emission in the innermost region, with $L_X = 1 \times 10^{40}$ erg s^{-1}, coincident with the super-bubble seen in optical images. The active nucleus may contribute to the emission as a point source.
– Emission from the disk of the galaxy, with $L_X = 7 \times 10^{39}$ erg s^{-1}, that can be partly resolved by the HRI in 3 point-like sources with luminosities of $\sim 6 \times 10^{38}$ erg s^{-1} each.
– Very soft X-shaped emission from the halo, with $L_X = 6 \times 10^{39}$ erg s^{-1}, extending to a diameter of 27 kpc.

The X-ray luminosity of NGC 3079 is higher by a factor of 10 compared to other galaxies of similar optical luminosity and we argue that this may be caused by the presence of an AGN rather than by starburst activity. The influence of the AGN on the companion galaxies in the NGC 3079 group are discussed.

Key words: galaxies: active – galaxies: individual: NGC 3079 – galaxies: jets – X-rays: galaxies

Table 1. Parameters of NGC 3079

		Ref.
Type	SBm	1
Assumed distance	17.3 Mpc (hence $1' \widehat{=} 5.0$ kpc)	2
Position of center (J2000.0)	R.A. $10^h01^m57\overset{s}{.}75$ Dec. $55°40'47''.0$	3
D_{25} diameter	$7'.7$	1
Corrected D_{25} diam.	$5'.5$	1
Axial ratio	0.22	1
P.A. major axis	166°	3
Inclination	84°	3
Galactic foreground N_H	0.8×10^{20} cm^{-2}	4

References: (1) Tully 1988, (2) Tully et al. 1992, (3) Irwin & Seaquist 1991, (4) Dickey & Lockman 1990

1. Introduction

The nearby spiral galaxy NGC 3079 is seen almost edge-on and has been investigated in detail at many wavelengths. Relevant galaxy parameters used throughout this paper are presented in Table 1. In optical light NGC 3079 shows disturbed morphology and dust lanes. The nuclear spectra indicate LINER/Seyfert 2 activity (Heckman 1980, Ford et al. 1986). In radio, NGC 3079 stands out for anomalous filamentary and bubble-like structure extending for ∼3 kpc along the minor axis to both sides of a bright compact nucleus (de Bruyn 1977, Seaquist et al. 1978, Hummel et al. 1983, Duric et al. 1983, Duric & Seaquist 1988). Extended radio emission also arises from the disk of the galaxy. A somewhat smaller loop of optical Hα emission (Ford et al. 1986, Duric & Seaquist 1988) or a super-bubble (Veilleux et al. 1994) appears associated with the eastern radio loop. With the help of optical long slit spectra these features have been interpreted as evidence of a super-wind powered by a nuclear starburst (Heckman et al. 1990) or an active nucleus (Filippenko & Sargent 1992). Veilleux et al. (1995) have further investigated the disk-halo connection in a detailed study of the diffuse ionized medium (DIM). They find that DIM contributes ∼30% of the total H_α emission of the galaxy disk within a radius of 10 kpc and that, within a radius of 5 kpc, X-shaped filaments rise for more than 4 kpc above the disk plane. Several bubbles and filaments within 1 kpc of the disk plane are interpreted as direct evidence for gas flow between the disk and halo. Within its distance, NGC 3079 is known to be one of the brightest sources of FIR continuum, CO line and H_2O maser emission (e.g. Henkel et al. 1984, Soifer et al. 1989, Irwin & Sofue 1992, Greenhill et al. 1995, Harwarden et al. 1995, Braine et al. 1997) reminiscent

Send offprint requests to: W. Pietsch
Correspondence to: wnp@mpe.mpg.de

of molecule and dust clouds and circumnuclear starburst activity. The H I distribution has been modeled by Irwin & Seaquist (1991), and slightly resolved H I and OH absorption was discovered against the radio core (Gallimore et al. 1994, Baan & Irwin 1995) indicative of a central mass within the inner 90 pc radius of more than $10^8 M_\odot$.

NGC 3079 is member of a group of galaxies consisting of the giant spiral, NGC 3079, and two small companions, MCG 9-17-9, 6.′5 to the NW, and NGC 3073 (= Mrk 131), 10′ to the SW (Irwin et al. 1987, Irwin & Seaquist 1991). MCG 9-17-9 is a small spiral of type Sb-Sc and NGC 3073 an early type (SAB0-) galaxy. While in the optical the two companions do not show signs of disturbance, in the radio NGC 3073 is found to exhibit an elongated H I tail which is aligned with the nucleus of NGC 3079, and the H I emission of MCG 9-17-9 is slightly extended in the direction of the nucleus of NGC 3079, too. An H II region spectrum coupled with deep Balmer absorption lines indicates that the stellar population of NGC 3073 is very young. Filippenko & Sargent (1992 and references therein) postulate that the copious star formation observed in NGC 3073 might have been triggered by the super-wind from NGC 3079 (see above), which, in projection, points in the direction of NGC 3073. From these observations it has been speculated by Irwin et al. that a hot inter-galaxy medium may be present in this group that might be observable in X-rays.

NGC 3079 was detected as an X-ray source by the Einstein observatory (Fabbiano et al. 1982, 1992) with a luminosity of 2.1×10^{40} erg s^{-1} in the 0.5–4 keV range (corrected to a distance of 17.8 kpc and for Galactic foreground absorption of 8.4×10^{19} cm^{-2}, and assuming a thermal bremsstrahlung spectrum with a temperature of 5 keV). ROSAT PSPC data of the galaxy have been analyzed by Reichert et al. (1994) and Read et al. (1997). They find an unresolved nuclear point source with a luminosity in the 0.1–2 keV band of 9.5×10^{39} erg s^{-1} and a diffuse emission component of 2.1×10^{40} erg s^{-1}. Dahlem et al. (1998) investigate the integral galaxy spectrum using ROSAT PSPC and ASCA data, and in addition present an overlay of ROSAT HRI contours over an H_α image of the center of the galaxy.

In this paper we present ROSAT HRI observation of NGC 3079 and a detailed reanalysis of the ROSAT PSPC data extracted from the ROSAT archive.

2. Observations and data analysis

NGC 3079 was observed from October 20 to 25, 1992 with the ROSAT HRI and from November 13 to 15, 1991 with the ROSAT PSPC, for a total observing time of 20.7 ks (HRI) and 19.0 ks (PSPC). The observations were split into 11 and 9 observation intervals (OBIs) for HRI and PSPC, respectively. To analyse the data for times of high detector background, we investigated rates of the master veto rate counter for the PSPC and the invalid counts for the HRI integrated over 60 s. The rates reach maxima of 280 cts s^{-1} (82 cts s^{-1}), but stay below 200 cts s^{-1} (60 cts s^{-1}) for 98% (99%) of the time for the PSPC (HRI). We therefore decided not to reject events due to times of high background.

2.1. Attitude corrections

To improve on the attitude solution we have adopted two subsequent techniques. For the HRI data we analyzed individual OBIs and aligned the data with the help of 7 bright point sources (namely H1, H2, H8, H9, H15, H20, H23, cp. Sect. 3.1) to the average position. While the offset in the position of these sources was $\leq3''$ for most OBIs, for OBI 5 the offset was $\sim12''$. The photons were corrected for the offsets.

We also looked for possible optical counterparts (see Appendix A.1 and A.2) with the aid of APM finding charts (Irwin et al. 1994), and compared the optical and X-ray positions, to determine a possible systematic error on the absolute attitude solution. We found optical candidates for 9 sources in the HRI and 7 in the PSPC. We determined a systematic shift of 3.″4 to the east and 3.″9 to the north and an additional counterclockwise rotation of 0.°39 for the HRI observation. The corrected center of the HRI pointing direction is $\alpha = 10^{\rm h}01^{\rm m}57^{\rm s}.2$, $\delta = 55^\circ42'39''.9$ (J2000.0). For the PSPC, we determined a shift of 8.″8 to the east and 6.″5 to the south and an additional counterclockwise rotation of 0.°2. The corrected center of the PSPC pointing is $\alpha = 10^{\rm h}01^{\rm m}56^{\rm s}.5$, $\delta = 55^\circ40'41''.5$ (J2000.0). Source lists and images have been corrected for these systematic effects. The remaining position uncertainty is less than 3″ for both instruments.

The attitude corrections determined above for HRI and PSPC are in good agreement with boresight parameters determined from a larger sample of observations that now are used for the SASS re-processing (M. Kürster, private communication).

2.2. Iso-intensity contour maps

For the PSPC data, contour plots have been obtained from images that were the result of the superposition of sub-images with 5″ bin size in the 8 standard bands (R1 to R8, cf. Snowden et al. 1994), corrected for exposure, vignetting, and dead time and smoothed with a Gaussian filter having a FWHM corresponding to the on-axis point spread function (PSF) of that particular energy band. The FWHM values used range from 52″ to 24″. The average background was calculated from a source free region to the north of NGC 3079.

For the HRI, contour plots have been obtained from images with 2.″5 bin size which were corrected for dead time and smoothed with a 12″ FWHM Gaussian filter. To reduce the background due to UV emission or cosmic rays we used only those events detected in the HRI raw Pulse Height Amplitude channels 2–8.

The resulting images are discussed in Sect. 3.1.

2.3. Source detection

We performed source detection and position determination with the EXSAS local detect, map detect, and maximum likeli-

Table 2. Conversion factors from count rates to fluxes (0.1–2.4 keV) for the ROSAT HRI and PSPC detector (broad band) in units of 10^{-11} erg cm^{-2} cts^{-1}, corrected for Galactic absorption

Temp.	THBR * 5 keV	THPL † 0.3 keV
HRI	3.95	3.56
PSPC	1.16	1.00

* thermal bremsstrahlung spectrum (we assumed $\mathrm{T} = 5$ keV for conversion of point-like sources)
† thin thermal plasma (we assumed $\mathrm{T} = 0.3$ keV for diffuse X-ray emission components)

hood algorithms (Zimmermann et al. 1992). Maximum likelihood values (L) can be converted into probabilities (P) through $\mathrm{P} \approx 1 - \mathrm{e}^{-\mathrm{L}}$, so that $\mathrm{L} = 8$ corresponds to a Gaussian significance of about 3.6σ and $\mathrm{L} = 10$ corresponds to a Gaussian significance of about 3.9σ (Cruddace et al. 1988; Zimmermann et al. 1994).

Once the count rates of sources are obtained (see below for the details on how they have been obtained in the two instruments), they are converted into fluxes in the ROSAT band (0.1–2.4 keV) assuming a 5 keV thermal bremsstrahlung (cf. Table 2). To estimate possible errors in the X-ray luminosities due to the selection of a wrong model or temperature, conversion factors for a 0.5 keV thermal bremsstrahlung and for a 0.3 keV and a 3 keV thin thermal plasma spectrum have also been calculated. For this range of temperature and models, the resulting values change by $\leq 15\%$.

Different considerations were applied to the HRI and the PSPC data to better suit the properties of these instruments.

HRI: Sources were searched for in the inner $\sim 37'$ diameter circle about the field's center. Again, we used only those events detected in the HRI raw Pulse Height Amplitude channels 2–8 (see Sect. 2.2). Sources with a $\mathrm{L} \geq 8$ were accepted.

PSPC: Sources were searched for in the inner $35' \times 35'$ field centered on NGC 3079 in the five standard ROSAT energy bands: "broad" (0.1–2.4 keV), "soft" (0.1–0.4 keV), "hard" (0.5–2.0 keV), "hard1" (0.5–0.9 keV), and "hard2" (0.9–2.0 keV). Sources for which we obtained $\mathrm{L} \geq 10$ in at least one of the bands were considered. We have used a slightly higher L value than in the HRI analysis since for the PSPC we are already getting background limited.

Once the existence of the source is established, its position is determined from the band with the highest L value. This is then used to derive the net counts in the five standard bands defined above in an aperture corresponding to $2.5\times$ FWHM of the energy band considered. The background is always taken from the same area in the corresponding background map (see EXSAS manual, Zimmermann et al. 1994). These values are used to calculate hardness ratios and their corresponding errors: HR1 = (hard–soft)/(hard+soft) and HR2 = (hard2–hard1)/(hard2+hard1), where all of the quantities are corrected for the appropriate vignetting correction (see EXSAS manual). If the source is not detected in one of the four bands, however, the corresponding hardness ratio cannot be simply calculated. We have therefore modified the algorithm, and determined to compute the hardness ratio using the 2σ upper limit instead of the net counts, when the signal-to-noise ratio in a particular band is less than 2. This allows us to estimate a maximum or minimum value that the hardness ratio can have. When both quantities are upper limits no hardness ratio is calculated.

Hardness ratios can be used to have a crude estimate of the spectral parameters that best apply to the energy distribution of the source photons, when the statistics do not allow a more detailed analysis. To show this we have also calculated "theoretical" hardness ratios from the spectral distribution of some standard spectral models ($i.e.$ Raymond & Smith, power law and thermal bremsstrahlung) with a low energy cut-off. These are shown in Fig. 1, and can be used as a comparison to the observed values of HR1 and HR2 (see Sects. 3.3.2 and Appendix A.1).

3. Results

3.1. Iso-intensity contour maps

A grey scale plot of the $21\farcm3 \times 21\farcm3$ HRI field is shown in Fig. 2. HRI sources found by the detection algorithms (see Sects. 2.2 and 3.2) are marked with their HRI number and a ellipse sketches the D_{25} (see Table 1).

Fig. 3 shows a contour map of the $30' \times 30'$ PSPC field centered on NGC 3079. The positions of all individual sources detected are marked, with their PSPC number. Note that P20 is detected only in the hard band, and does not appear in the broad-band map. The ellipse sketches the D_{25}.

A smaller portion of the HRI field corresponding to the area of the extended emission seen with the PSPC is presented in Fig. 4. The HRI spatial resolution resolves the emission from the galaxy's plane into a structure at the center and three individual sources, but is not sensitive enough to show the low surface brightness emission at large galactocentric radii.

Fig. 10 (see Sect. 4) shows the inner part of the PSPC field superposed onto the optical image of the galaxy. It is immediately apparent that the emission from NGC 3079 is complex and extends both above and below the galaxy's plane. We have also produced maps of the emission in different energy ranges (Fig. 5), namely in the soft, hard1 and hard2 bands defined above. As can be seen by the comparisons of the iso-intensity contour maps, the softer and harder emission show rather different morphologies. The hard2 band emission is aligned with the optical disk of the galaxy, and seems to be rather confined to it, while both the hard1 and the soft images show extensions above and below the plane. This difference cannot be attributed to the different response of the instrument in the different energy bands and indicates the presence of more than one component to the emission of NGC 3079 (see discussion later).

3.2. HRI/PSPC sources in the field

The source detection procedure yielded 23 sources in the HRI and 34 in the PSPC above the selected likelihood threshold for

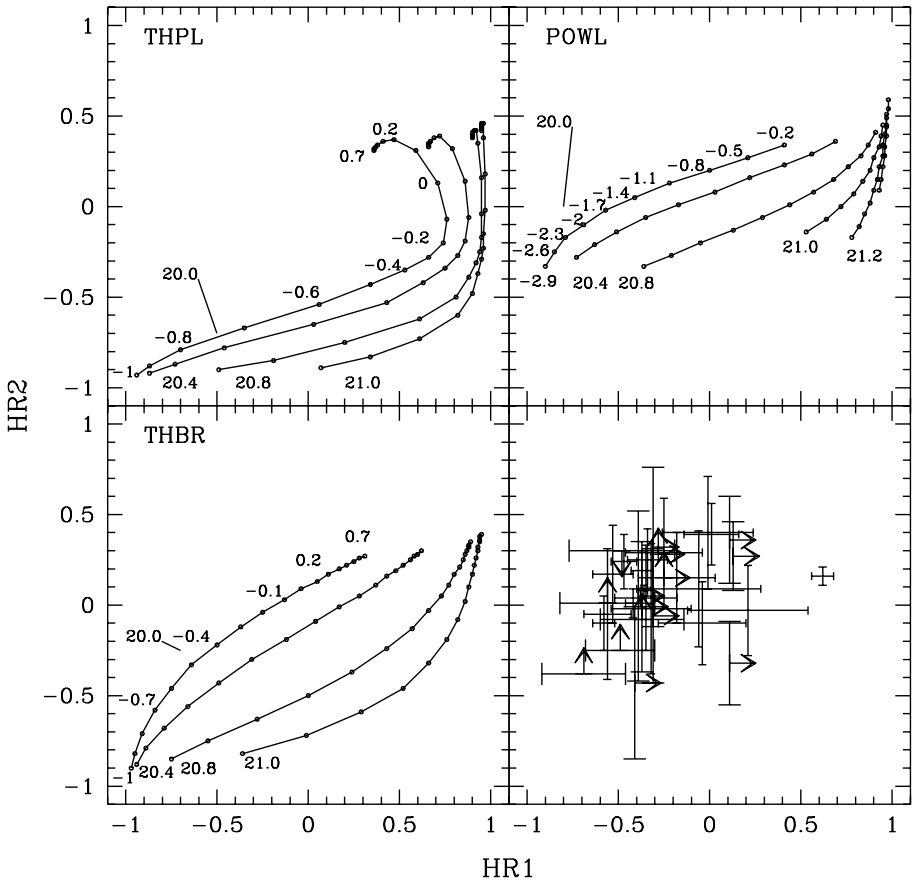

Fig. 1. Expected distribution of HR1 and HR2 for different spectral models and spectral parameters and observed values. Curves are drawn for different assumed equivalent absorbing column, as given in the figure (in logarithmic value) and for different temperatures/indexes. Left panels: Curves for Raymond & Smith (top) and thermal Bremsstrahlung spectra. Dots along the curves indicate different temperatures, in steps of 0.1 in log(T_7), where T_7 is $T/10^7$ K. Some of the points are labeled for easy reference. Upper right pannel: Curves for power law spectra. Dots along the curves indicate different photon index, as indicated. Lower right pannel: Observed hardness ratios and limits

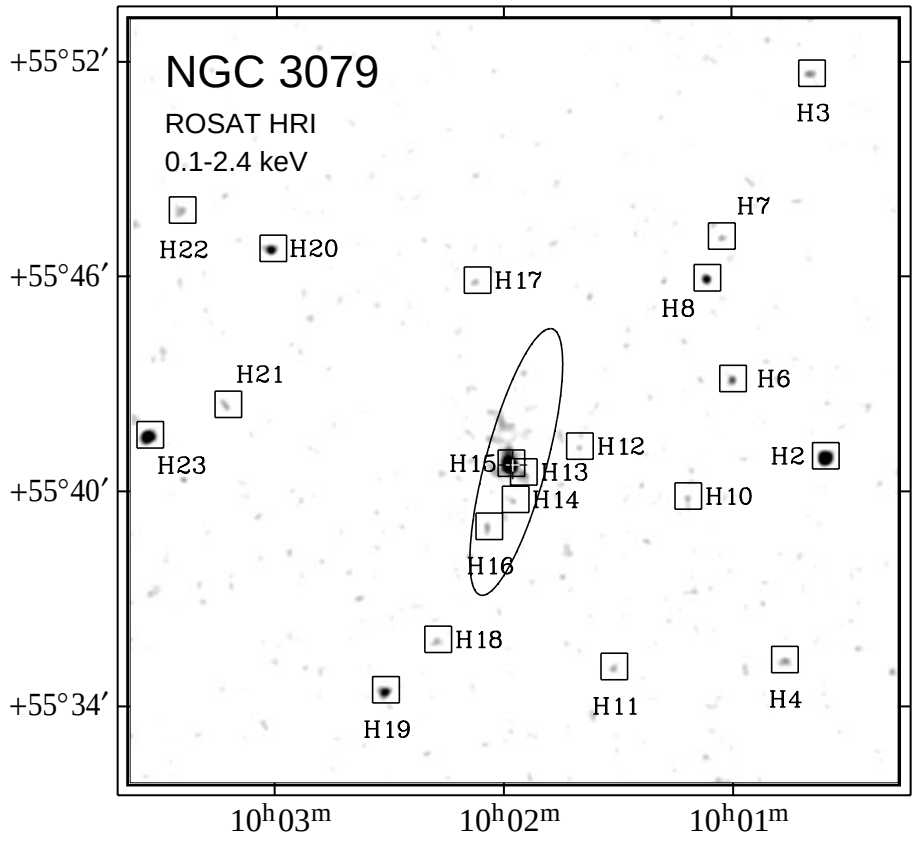

Fig. 2. Grey scale plot of the inner $21\farcm3 \times 21\farcm3$ X-ray image seen with the ROSAT HRI. The image was constructed with a pixel size of $2\farcs5$ and smoothed with a Gaussian of $12''$ (FWHM). The center of NGC 3079 is marked with a cross, the D_{25} ellipse is indicated, and point sources (likelihood $L \geqq 8$) are enclosed by boxes and numbered (see Table 3). Right ascension and declination are given for J2000.0

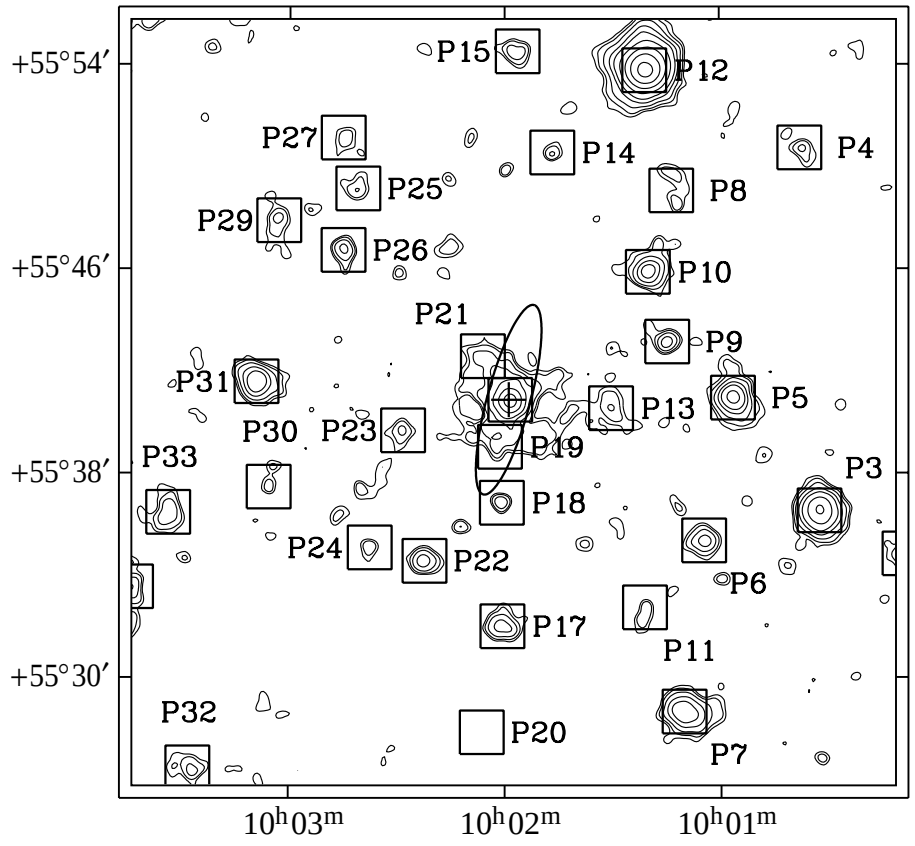

Fig. 3. Contour plot of the broad band ROSAT PSPC image of the inner $30' \times 30'$ of the NGC 3079 field (cf. Sect. 2.2 for how the image was constructed). Contours are 2, 3, 5, 9, 15, 31, 63, 127, and 255σ above the background ($1\sigma \mathrel{\widehat{=}} 462 \times 10^{-6}$ cts s^{-1} arcmin^{-2}, background $\mathrel{\widehat{=}} 2490 \times 10^{-6}$ cts s^{-1} arcmin^{-2}). ROSAT PSPC detected sources (likelihood L $\geqq$ 10) are plotted as squares with source numbers written alongside (see Table 4). The position of the nucleus of NGC 3079 is marked as a cross, the optical extent is indicated by the ellipse at D_{25}. P16 detected close to the galaxy center, has not been numbered

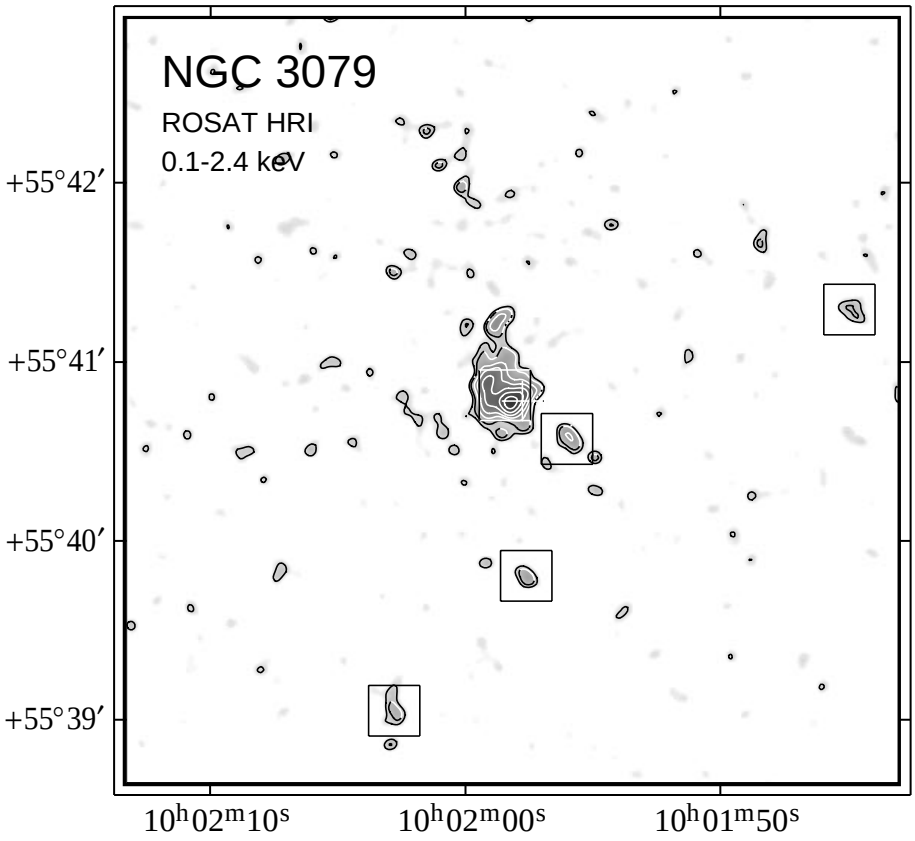

Fig. 4. Contoured grey scale plot of the central emission region of NGC 3079 for ROSAT HRI. The image is binned to a $1''$/pixel and smoothed with a Gaussian function with FWHM=$5''$. Contours are given in units of 0.5 photons accumulated per $4''.7$ diameter. Contour levels are 3, 5, 9, 15, 31, 63 units. The center of NGC 3079 is marked by a cross, HRI detected point sources by squares

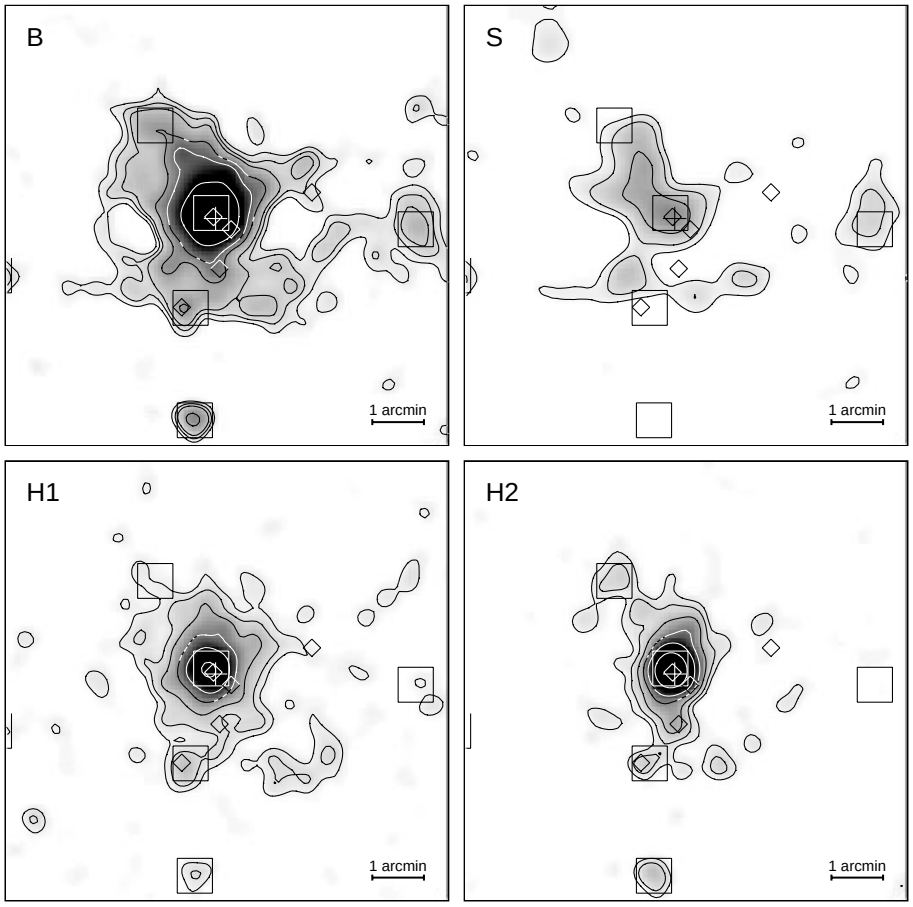

Fig. 5. Contour plots of the central emission region of NGC 3079 for broad (B), soft (S), hard1 (H1), and hard2 (H2) ROSAT PSPC bands. Broad band contours are given as in Fig. 3. Soft band contours are given in units of σ (375×10^{-6} cts s^{-1} arcmin^{-2}) above the background (1905×10^{-6} cts s^{-1} arcmin^{-2}), hard band contours (due to the negligible background in these bands) in units of 1 photon accumulated per 24″ diameter. One unit $= 418 \times 10^{-6}$ cts s^{-1} arcmin^{-2} for the hard bands. Contour levels are 2, 3, 5, 9, 15, 30 units for all contour plots. A cross indicates the center on NGC 3079, squares indicate the positions of the PSPC detected sources in the field, diamonds of HRI detected sources

source existence. These numbers reduce to 20 sources in the inner $21\farcm3 \times 21\farcm3$ HRI field (Fig. 2) and 30 sources in the inner $30' \times 30'$ of the PSPC image (Fig. 3).

The X-ray properties of the sources are summarized in Tables 3 and 4: source number (col. 1), ROSAT name (col. 2), right ascension and declination (col. 3, 4), error of the source position (col. 5, including the 3″ systematic error for the attitude solution), likelihood of existence (col. 6), net counts and error for the 0.1–2.4 keV ROSAT band (col. 7), count rates and error after applying dead time and vignetting corrections (col. 8). For PSPC sources we also list hardness ratios HR1 and HR2 with their relative errors (col. 9, 10). For PSPC sources, positions and maximum likelihood values have been determined from the energy band with the highest detection likelihood, but the count rates refer to the broad band. To distinguish HRI from PSPC sources, a H or a P has been prefixed to the number for HRI or PSPC, respectively. For sources detected in both instruments, the ROSAT names have been derived from the detection with the smaller error radius. These were mainly HRI detections. Only for two sources (H1 and H5) the HRI position errors are bigger than the corresponding PSPC errors due to source variability or big off-axis angle (see Sect. A.1).

Only one HRI source (H15, at the center of NGC 3079) and two PSPC sources (P16, at the center of NGC 3079, and P28) were flagged as extended by the maximum likelihood detection algorithm.

Besides for the galaxy's center, only one other PSPC source, P19, and 3 HRI sources, H13, H14, and H16, are positioned within the D_{25} contours of the galaxy. However it is likely that also sources H12, H18, P18, and P21, are related to NGC 3079, and they will be regarded as such in what follows (see Sect. 3.3). Moreover, it is also possible that some of these sources, located in this complex area where extended emission is also seen, are spurious detections picked up by the detection algorithms as a consequence of a bad background model due to the more diffuse component and represent local enhancements. One HRI source (H6) and the corresponding PSPC source P9 are identified with the companion galaxy MCG 9-17-9 (see Sect. 3.5). Properties of other sources outside the D_{25} ellipse of NGC 3079 are discussed in the appendix.

3.3. The emission from NGC 3079

Complex emission partially filling the D_{25} ellipse and extending into the halo along the minor axis is detected (see Figs. 2, 3, 4, and 5). On top of this emission, the central nuclear region and five sources (H12, H13, H14, H16/P19, P21) are resolved. Two additional sources (P18, and H18) positioned outside the D_{25} diameter are within the H I envelope of NGC 3079, and are also probably associated to the emission of NGC 3079. The properties of the nuclear source (H15/P16) are further investigated in Sect. 3.4. The two sources H13 and H14 detected with the HRI

Table 3. X-ray properties of the sources detected with the HRI in a $\sim 37'$ diameter field centered on NGC 3079

(1)	*ROSAT* name (RX J) (2)	RA (2000) (h m s) (3)	Dec (2000) (° ′ ″) (4)	R_{err} (″) (5)	Lik. (6)	Net counts (7)	Count rate (10^{-4} s^{-1}) (8)	PSPC source n. (9)
H1	100032.3+553631*	10 00 32.2	55 36 31	4.4	201.2	160.2±14.2	84.7± 7.5	P3
H2	100056.4+554100	10 00 56.4	55 41 01	3.5	167.8	88.1± 9.9	44.6± 5.0	P5
H3	100058.9+555141	10 00 59.0	55 51 42	8.4	10.0	18.3± 5.7	9.5± 2.9	
H4	100104.7+553519	10 01 04.8	55 35 19	8.2	9.9	17.6± 5.5	9.1± 2.9	P6
H5	100110.0+552838*	10 01 09.6	55 28 27	10.9	18.3	43.9± 9.5	23.8± 5.1	P7
H6	100114.6+554310	10 01 14.6	55 43 11	4.1	23.2	16.8± 4.5	8.4± 2.2	P9
H7	100116.8+554709	10 01 16.8	55 47 09	5.2	9.5	10.5± 3.8	5.3± 1.9	
H8	100119.7+554559	10 01 19.7	55 45 59	3.7	44.6	25.5± 5.4	12.7± 2.7	P10
H9	100120.6+555355	10 01 20.6	55 53 56	3.1	2118.4	712.6±27.3	369.9±14.1	
H10	100123.5+553953	10 01 23.5	55 39 54	5.1	8.2	8.9± 3.5	4.4± 1.7	P12
H11	100138.2+553508	10 01 38.2	55 35 08	6.4	8.3	11.2± 4.2	5.7± 2.1	
H12	100144.9+554117	10 01 44.9	55 41 18	4.7	8.4	8.3± 3.3	4.1± 1.6	
H13	100156.1+554034	10 01 56.2	55 40 34	4.3	14.4	11.6± 3.8	5.7± 1.9	
H14	100157.6+553948	10 01 57.6	55 39 49	4.4	9.0	7.7± 3.1	3.8± 1.5	
H15	100158.5+554049	10 01 58.6	55 40 49	3.5	127.0	113.3±11.2	55.6± 5.5	P16
H16	100202.8+553903	10 02 02.9	55 39 03	4.5	10.4	9.1± 3.4	4.5± 1.7	P19
H17	100205.0+554555	10 02 05.0	55 45 56	4.5	8.7	7.6± 3.1	3.7± 1.5	
H18	100212.9+553553	10 02 13.0	55 35 54	5.5	9.4	11.1± 4.0	5.6± 2.0	
H19	100223.0+553429	10 02 23.0	55 34 29	4.8	37.1	33.4± 6.6	17.0± 3.4	P22
H20	100245.5+554648	10 02 45.6	55 46 49	3.9	49.5	31.4± 6.0	15.8± 3.0	P26
H21	100254.2+554226	10 02 54.2	55 42 27	6.9	8.7	11.5± 4.2	5.8± 2.1	
H22	100303.4+554752	10 03 03.4	55 47 52	6.9	13.3	19.5± 5.5	10.0± 2.8	P29
H23	100309.6+554135	10 03 09.6	55 41 35	4.0	108.8	72.3± 9.2	36.9± 4.7	P31

* The more accurate PSPC position is used to name this source

are too close to the bright nucleus (25″ and 60″, respectively) to be resolved by the PSPC. The HRI source detection algorithm did not separate a source at the northern end of the diffuse central emission (distance 25″), even though the contour map of Fig. 4 suggests a separate peak. Sources P13 and H10 appear to be within the outermost PSPC contour of Fig. 3. While at the present time it is not possible to exclude the possibility that these are unrelated background sources, the evidence of excess emission in this region suggests that maybe these are the peaks of a more extended emission probably connected with the galaxy or with the group. We therefore will discuss these two sources as both truly individual sources and as a more diffuse component.

Table 5 summarizes PSPC and HRI count rates, X-ray fluxes f_X and luminosities L_X of the sources in NGC 3079. For two sources that were detected only in the PSPC, and for 2 detected in the HRI only, a 2σ limit to the HRI (PSPC) count rates at the same positions are calculated. These are estimated from circles of radii of $0.75\times$ FWHM of the source at the off-axis distance (PSPC and HRI, respectively). The fluxes are then corrected by a factor 2 to compensate for the small aperture used to estimate the net counts. No equivalent limit is given for H13 and H14, since they would not be resolved in the PSPC.

While the luminosity of the nuclear source is above 8×10^{39} erg s^{-1} most of the other sources are close to the detection limit and show luminosities in the range $(5-12)\times 10^{38}$ erg s^{-1}.

The count rates of the individual sources in NGC 3079 are too low to be used to study time variability within each individual PSPC or HRI observation (day time scale). We can however investigate time variability of the sources on one year time scale by comparing the PSPC and HRI observations that were taken $\sim$ 1 year apart. No source variability can be claimed for the sources in NGC 3079.

The 2σ HRI upper limit for source P21 however appears to be significantly lower than the PSPC flux. P21 is detected from the algorithm in the hard2 band only, as can also be seen by the maps in Fig. 5. While it is at the moment unclear whether this should be considered a real source, or rather a local enhancement in the diffuse emission that extends to the NE of the galactic plane, it is clear that a variability study is severely hampered by the presence of this latter component, given the widely different spatial resolutions and sensitivity to low surface brightness components of the HRI and the PSPC. Therefore the much lower HRI flux could be in part (totally) due to the different amounts of diffuse component in the detection cell. In fact, when we estimate the background locally, namely from the average surface brightness of the emission at the same radial distance from the center, the net count rate above the extended emission reduces to almost a half, and the flux $f_x \sim (1.7\pm0.7)\times 10^{-14}$ erg cm^{-2} s^{-1}, comparable to the upper limit determined from the HRI data.

Table 4. X-ray properties of sources detected with the PSPC in a $35' \times 35'$ field centered on NGC 3079

	ROSAT name (RX J)	RA (2000) (h m s)	Dec (° ′ ″)	R_{err} (″)	Lik.	Net counts	Count rate (10^{-3} s^{-1})	HR1	HR2
(1)	(2)	(3)	(4)	(5)	(6)	(7)	(8)	(9)	(10)
P1	095956.3+554639	09 59 56.4	55 46 40	17.6	20.4	74.2±13.6	4.5±0.8	−0.5±0.2	≥ −0.3
P2	100008.8+553448	10 00 08.9	55 34 49	18.8	15.2	60.0±13.2	3.6±0.8	−0.3±0.2	0.0±0.4
P3	100032.3+553631	10 00 32.4	55 36 31	4.2	888.7	640.2±28.0	37.2±1.6	−0.4±0.1	−0.0±0.1
P4	100037.4+555046	10 00 37.4	55 50 47	18.1	20.2	46.1±11.1	2.7±0.7	0.2±0.3	0.0±0.3
P5	100056.4+554100*	10 00 56.4	55 40 58	4.7	340.7	297.7±19.9	16.7±1.1	−0.4±0.1	0.2±0.1
P6	100104.7+553519*	10 01 04.6	55 35 22	9.5	40.7	82.0±12.7	4.6±0.7	−0.2±0.2	0.2±0.3
P7	100110.0+552838	10 01 10.1	55 28 39	6.5	245.4	288.3±20.5	17.0±1.2	−0.6±0.1	−0.1±0.2
P8	100113.3+554906	10 01 13.4	55 49 06	25.6	15.7	56.2±14.8	3.2±0.8	> 0.1	−0.3±0.2
P9	100114.6+554310	10 01 14.6	55 43 10	7.0	62.0	68.8±11.3	3.8±0.6	> 0.1	0.3±0.2
P10	100119.7+554559*	10 01 19.9	55 45 55	6.2	128.0	154.1±15.3	8.6±0.9	−0.3±0.1	0.3±0.2
P11	100120.9+553244	10 01 20.9	55 32 44	19.5	12.5	29.2± 9.4	1.6±0.5	> −0.3	−0.1±0.4
P12	100120.6+555355*	10 01 20.9	55 53 50	3.2	8066.9	2957.6±55.8	173.1±3.3	−0.4±0.1	0.1±0.1
P13	100130.2+554033	10 01 30.2	55 40 34	25.7	11.5	57.4±13.8	3.1±0.8	−0.7±0.2	> −0.4
P14	100146.6+555036	10 01 46.6	55 50 36	14.7	10.2	33.1± 9.3	1.9±0.5	> −0.4	0.1±0.5
P15	100156.3+555434	10 01 56.4	55 54 35	12.4	24.1	61.5±11.7	3.6±0.7	−0.4±0.2	> −0.1
P16	100158.5+554049*	10 01 58.3	55 40 53	4.7	1022.0	643.4±28.5	35.2±1.6	0.6±0.1	0.2±0.1
P17	100200.5+553200	10 02 00.5	55 32 00	9.0	67.0	113.6±14.0	6.4±0.8	−0.5±0.1	0.2±0.3
P18	100200.7+553651	10 02 00.7	55 36 51	9.6	20.5	44.0± 9.9	2.4±0.5	> −0.3	> 0.1
P19	100202.8+553903*	10 02 01.2	55 39 03	11.9	25.3	37.2± 9.9	2.0±0.5	0.0±0.2	−0.1±0.2
P20	100206.2+552750	10 02 06.2	55 27 50	21.8	10.4	16.4± 8.7	1.0±0.5	> −0.4	0.0±0.4
P21	100206.0+554236	10 02 06.0	55 42 36	14.9	14.6	46.0±10.8	2.5±0.6	−0.2±0.2	0.3±0.3
P22	100223.0+553429*	10 02 22.3	55 34 34	8.2	51.5	88.4±12.5	4.9±0.7	−0.3±0.2	0.0±0.3
P23	100228.2+553941	10 02 28.3	55 39 41	15.3	10.7	37.7±10.1	2.1±0.6	< −0.2	–
P24	100237.4+553505	10 02 37.4	55 35 05	14.8	10.4	30.9± 9.4	1.7±0.5	> −0.4	−0.4±0.4
P25	100240.8+554910	10 02 40.8	55 49 11	16.4	12.0	42.0±10.7	2.4±0.6	−0.5±0.3	< 0.3
P26	100245.5+554648*	10 02 44.9	55 46 46	8.4	44.4	65.9±11.3	3.7±0.6	> 0.1	0.4±0.2
P27	100244.9+555110	10 02 44.9	55 51 11	17.9	10.0	33.5±10.1	1.9±0.6	> −0.3	> 0.3
P28	100245.1+555758	10 02 45.1	55 57 59	12.9	111.3	241.9±21.3	14.9±1.3	0.0±0.2	0.4±0.2
P29	100303.4+554752*	10 03 02.9	55 47 55	20.1	15.1	45.5±11.1	2.6±0.6	−0.1±0.3	0.1±0.3
P30	100305.5+553727	10 03 05.5	55 37 28	13.3	16.4	24.2± 8.7	1.4±0.5	> −0.3	0.3±0.4
P31	100309.6+554135*	10 03 09.1	55 41 36	5.8	207.8	221.9±17.8	12.6±1.0	−0.5±0.1	> 0.0
P32	100327.8+552625	10 03 27.8	55 26 26	28.7	10.9	51.7±13.0	3.2±0.8	−0.6±0.3	> 0.0
P33	100333.5+553627	10 03 33.6	55 36 27	14.0	29.8	79.1±13.3	4.7±0.8	−0.6±0.1	−0.1±0.4
P34	100343.6+553331	10 03 43.7	55 33 31	16.9	24.8	68.4±12.5	4.2±0.8	0.0±0.3	0.4±0.3

* The more accurate HRI position is used to name this source

3.3.1. Radial distribution of the emission

To determine the extent of the emission and the spatial distribution of the detected photons we have produced radial surface brightness plots from the PSPC and from the HRI data, centered at the X-ray central peak (sources P16 or H15). The plots are shown in Fig. 6. The radial distribution of a point source, at the central position, binned as the data and normalized to them in the innermost bin, is also plotted for comparison. In the PSPC data, the point source is simulated separately in energy bins of 0.1 keV which are then normalized to the count rates in the relevant sub-band and co-added. In the HRI data, it is obtained from the analytical formula given in David et al. (1994) for a source on-axis. In both HRI and PSPC data, the overall photon distribution is inconsistent with a point source (however, see later for further analysis of the HRI data).

The azimuthally averaged surface brightness distribution of the emission (Fig. 6) extends out to a radius of r $\sim 2'.7$ (13.5 kpc) in the PSPC data, outside of which the profile becomes constant with radius and consistent with the background map created from the data (see Sect. 2.3). Similar plots in the soft and hard band indicate maximum radii of comparable values. In the HRI, the profile flattens at a radius r $\sim 2'$ (10 kpc). For the HRI, we can therefore determine the field background from a region outside of the galaxy's emission by choosing an annular region around the galaxy of $4' - 6'$ inner and outer radii, respectively. Point sources that lie in the background regions have not been included for background estimates by masking them out with

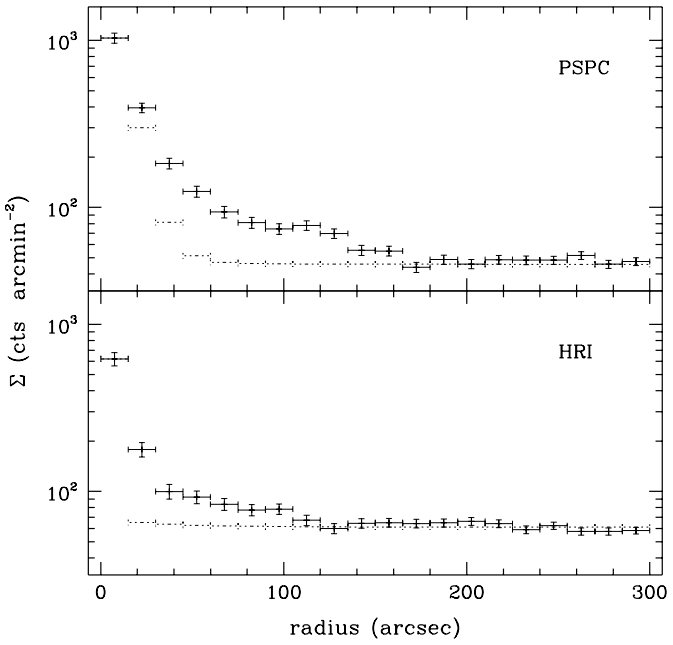

Fig. 6. Radial distribution of the detected photons, azimuthally averaged in concentric annuli of 15″ width. The dashed profiles indicates the radial distribution of a point source and the background level estimated as explained in the text. Point sources detected have not been removed from these profiles

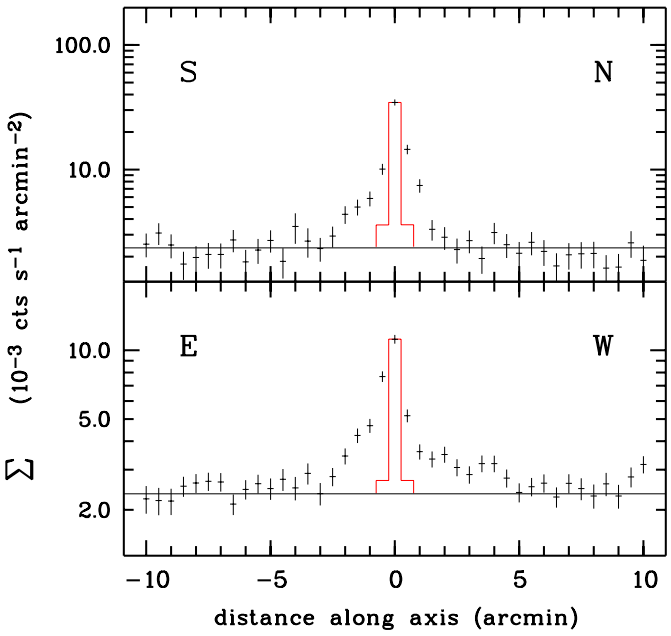

Fig. 7. Spatial distributions of the surface brightness along the major (above) and minor (below) axis of NGC 3079. ROSAT PSPC counts are integrated in boxes of $30'' \times 60''$ along the major axis, covering the galaxy disk region, and in boxes of $30'' \times 300''$ along the minor axis, covering the galaxy halo region. They are centered at the distance given on the X axis relative to galaxy's nucleus. All PSPC sources (except P13, P16, P19, and P21 probably connected to the galaxy) have been cut out with a cut radius of $2\times$ FWHM of PSF at 0.3 keV. Response of a point source at the nucleus of NGC 3079 is given as dotted histogram (normalized to the count rate of the central box)

Table 5. X-ray parameters of NGC 3079 sources

Number HRI	Number PSPC	Δ (″)	Flux HRI *	Flux PSPC *	L_X HRI **	L_X PSPC **
(1)	(2)	(3)	(4)	(5)	(6)	(7)
H12			1.6±0.6	< 3.4	5.8	< 15
H13			2.2±0.7		8.1	
H14			1.5±0.6		5.4	
H15	P16	5.0	22.0±2.2	40.8±1.9	78.8	146.2
	P18		< 2.6	2.8±0.6	< 9.2	10.0
H16	P19	15.0	1.8±0.7	2.3±0.6	6.4	8.3
H18			2.2±0.8	2.0±1.0	8.1	7.1
	P21		< 1.8	2.9±0.7	< 6	10.4

* fluxes in units of 10^{-14} erg cm^{-2} s^{-1} for a 5 keV thermal bremsstrahlung spectrum in the 0.1–2.4 keV band, corrected for Galactic absorption

** luminosity in units of 10^{38} erg s^{-1} assuming a distance of 17.3 Mpc. Fluxes and luminosities (for which errors are not quoted) of these sources, in particular for the PSPC data, should be taken with caution, since extended diffuse emission is included in the flux of the individual sources due to the relatively large dimension of the instrument point spread function (see text)

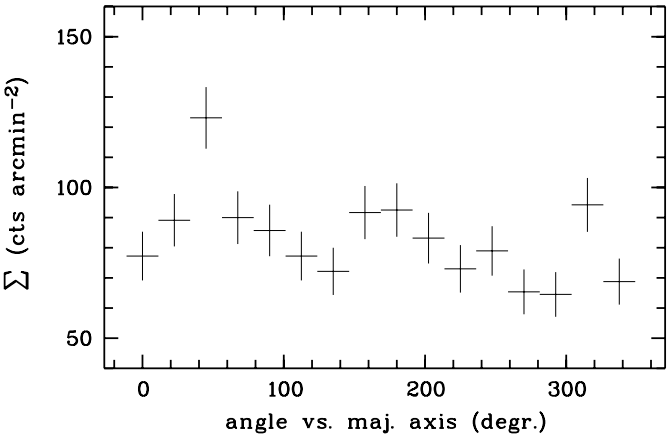

Fig. 8. Azimuthal distributions of the surface brightness of NGC 3079. ROSAT PSPC counts are integrated over sectors of 22.5 degree within a radius of 2.′5. The central source has been cut out with 30 ″ radius. The sector at 0° is centered at the direction of the major axis and angle is counted from north to the east

circles of 30″ and 15″ radii for PSPC and HRI, respectively. Correction for vignetting is negligible at these off-axis angles.

Given the presence of P13 in the PSPC data, and of the apparent connection between this source and the galaxy (see Fig. 10), we have further analyzed the PSPC data by looking at the radial distribution of photons in different directions and in comparison to the expected pure field background, whose shape is represented by the exposure map. In fact, while the background map is constructed from the data and therefore takes partially into account any diffuse emission present in the field, the exposure map should represent the PSPC response to a flat,

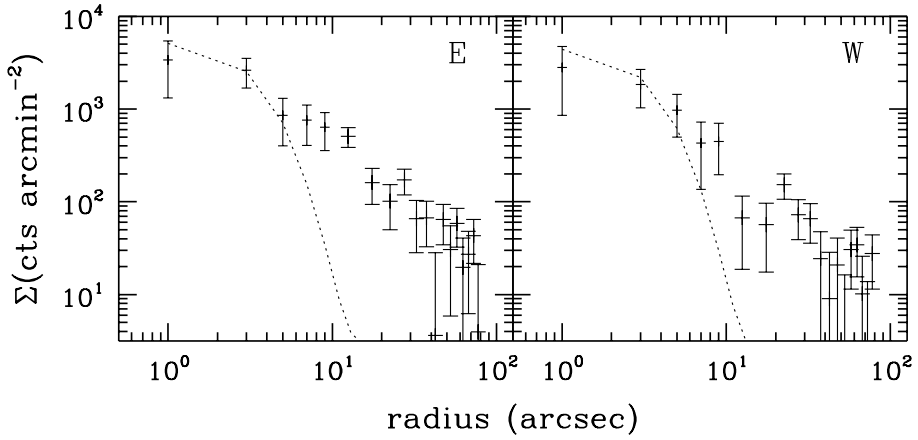

Fig. 9. Radial profiles of the HRI X-ray surface brightness of NGC 3079 in two opposite halves. The dotted line indicates the profile expected for a point source arbitrarily normalized to the $+1\sigma$ value of the innermost point

constant radiation, while taking into account both exposure and vignetting. When properly normalized to the data, the expected field background can therefore be estimated from it (see also Trinchieri et al. 1994, Kim & Fabbiano 1995). Fig. 7 shows the results of the comparison between the spatial profiles in different directions relative to the exposure map. These have been obtained by calculating surface brightness profiles along the major and minor axis using boxes of $30'' \times 60''$ and $30'' \times 300''$, respectively, perpendicular to the axis. Sources P5, P6, P14, P17, P18, P22, P23 and P31 were cut out with a cut radius of $2\times$ FWHM of PSF at 0.3 keV. We normalized according to box area and exposure and corrected for vignetting and dead time. The normalization of the exposure map is determined at $8'$ to $10'$ offset from the galaxy.

The profiles along the major and minor axes are clearly more extended than a point source (cf. Fig. 7). The extent along the major axis ($\sim$2.′5 corresponding to 12.5 kpc to both sides of the nucleus) is similar to the optical (about the corrected D_{25}). If the X-ray emission only originated from the galaxy disk, given the galaxy's inclination one would expect a $\leq 1'$ extent to both sides of the nucleus along the minor axis. Fig. 7 instead shows an extension comparable to that along the major axis and possibly more. In the Western direction, excess emission is detected out to $\sim 6'$ (30 kpc), while only a marginal excess is seen at distances greater than 2.′5 (12.5 kpc) in the Eastern direction.

We can quantify this excess by noticing that $\sim 221 \pm 32$ net excess counts are found in the region from $2.'5 - 6'$ in the western direction, significantly higher than the expected contribution from the single source P13 ($\sim$ 57 counts, from Table 4) and also much more extended than expected from a single point-like source. While with the present data we cannot exclude that P13 is indeed an individual source, the excess found points towards interpreting it as a local enhancement onto a somewhat irregular emission. No optical counterpart can be seen in the finding charts (see Appendix A.2). The excess in the east is $\sim 49 \pm 26$ net excess counts. For comparison, we can measure no excess ($\sim -30 \pm 21$ and $\sim -6 \pm 29$ counts) in the N and S directions along the major axis in the same area and at the same radial distance from center.

Asymmetries and irregularities in the emission are also found on smaller scales. Outside of the nuclear area, an almost X-shaped emission (the arm to the SE of the major axis is not as evident as the others) is detected, as indicated rather irregular azimuthal surface brightness distribution outside of the nuclear area shown in Fig. 8. In particular, there are two enhancements relative to neighboring sectors at $\sim \pm 45^\circ$ from the major axis, and clear depressions in the direction almost perpendicular to the major axis ($\sim 13^\circ$ and 270° in Fig. 8).

To better study the presence of an unresolved core in the data, we have further analyzed the HRI data, and we have produced radial profiles of the net emission in two opposite halves, *i.e.* East and West. As shown by Fig. 9, where the comparison with the PSF is also shown, there is a suggestion for the presence of an unresolved source embedded in a more extended component, and a significantly steeper decline in the Western half of the plane than the Eastern half. However, the point-source component does not dominate in the inner $20'' - 30''$ radius region, so any attempt to study it at the PSPC resolution is hampered by the presence of the extended component.

3.3.2. Spectral analysis

The morphology of the emission from NGC 3079, coupled with its optical and H I properties, suggests that the X-ray emission comes from three separate regions with presumably very different characteristics. The bright central region ($60''$ diameter), resolved in a complex source plus 2 point-like sources by the HRI, is likely to experience a large absorption. Similarly, the emission from the disk, seen edge-on, will be heavily absorbed, with the exception of the very external layers. In the halo region, instead, absorption consistent with the line of sight H I column density from our own galaxy is expected. A possible difference between the two sides of the plane, as the galaxy is not perfectly edge-on, might also be expected. In addition, inter-galaxy gas within the group (see introduction) may add additional absorption.

Given the limited statistics offered by the PSPC data, we have tried to minimize the number of separate regions from which to extract the photons for spectral analysis purposes.

Table 6. Extracted spectra. Source plus background region (and covered area) as well as background region are given

Spectrum	Source region	Area (arcmin^2)	Background region	Net counts	HR1	HR2
all	0 to 5.′5 diameter around the center of the galaxy	23.76	8′ to 12′ diameter after screening point sources with a cut diam. of 60″	1142±57.4	0.49±0.06	0.03±0.04
central	0 to 60″ diameter around central X-ray emiss. peak	0.79	see *all*	401±21.7	0.79±0.05	0.21±0.05
clocal	see *central*	0.79	60″ to 90″ diam. around central X-ray emiss. peak	290±24.1	0.86±0.07	0.33±0.08
disk	box from 0.′6 E to 0.′6 W along minor axis, from 2.′0 N to 2.′3 S along major axis, *central* excluded	4.45	see *all*	286±26.4	0.77±0.12	−0.08±0.07
halo	2 boxes: 0.′6 E to 2.′6 E; 0.′9 N to 2.′3 S and 0.′6 W to 2.′1 W; 2.′0 N to 2.′3 S	12.83	see *all*	349±38.8	0.08±0.12	−0.17±0.11

We have therefore checked with the aid of the hardness ratios whether different regions showed significantly different spectral characteristics, as could be expected from the considerations above. HR1 and HR2 have been calculated as defined in the previous section for 4 different regions:

a) the central region, defined as a circle of 30″ radius, centered at α=$10^{\rm h}01^{\rm m}58\overset{\rm s}{.}3$ and δ=55°40′53″ (J2000.0)
b) the disk region, defined as a box of size $73'' \times 260''$, positioned along the major axis of the galaxy, shifted 20″ to S. The central source region has been masked out in the count extraction (cut radius 30″)
c) the halo region above the plane, defined as a box of size $3.'2 \times 2.'0$, positioned parallel and adjacent to the E of the disk region
d) the halo region below the plane, defined as a box of size $4.'3 \times 1.'5$, positioned parallel and adjacent to the W of the disk region

The background was taken from an annulus of 4′ and 6′ inner and outer radii respectively, centered at the X-ray peak position (source P16).

We found no significant difference between the hardness ratio values for regions c) and d), and we have therefore defined as $halo$ region the combination of c)+d) above. Table 6 summarizes the definitions of source and background regions used to determine hardness ratios and photon energy distributions for spectral fitting. As shown by Table 6, we have also considered the galaxy as a whole, and we have used a local background for the central region, to take into account possible contamination from the disk.

Comparison of the HR1 and HR2 values and also with the $theoretical$ hardness ratios shown in the plots of Fig. 1 clearly indicate that the central region, the disk and the halo occupy different regions of the HR1/HR2 diagram. We have then used simple spectral models to fit the data in the different regions, as indicated in Table 7. Raw spectra have been rebinned to obtain at least the signal to noise level per bin given in col. 1 of Table 7. Rough errors for the fluxes and luminosities in Table 7 are indicated by the statistical errors on the net counts (see Table 6, although additional uncertainties come from the poor knowledge of the spectrum, as can be seen by simply comparing the fluxes derived for different models).

It is apparent that in all cases but the halo region, power law and thermal bremsstrahlung models give a better approximation of the data than the thin plasma model (Raymond-Smith code). Moreover, this latter would prefer a low energy absorption $below$ what is expected from the line-of-sight H I column density, without giving a significant improvement in the best fit χ^2 value. Power law or thermal bremsstrahlung models give essentially equivalent goodness of fit, and produce spectral models that are a good approximation of the energy distribution of the detected photons. In all cases a significant amount of intrinsic absorption above the line-of-sight value of 8×10^{19} cm^{-2} is suggested, consistent with the idea that the emission comes from within the galaxy, and therefore suffers from the absorption in NGC 3079 itself. The fact that we have obtained very similar results from the disk and central regions is not surprising since, as already remarked above, the extended emission contributes significantly even at small radii, and this, combined with the extremely poor statistical significance of the data, does not allow us to distinguish the presence of a different component (for example from the point source in the nuclear region suggested by the HRI data).

Even though a good fit is already obtained for power law and thermal bremsstrahlung models, for the galaxy as a whole we have also tried to improve on the best fit values in the thin

Table 7. Spectral investigations of the extracted spectral files

Spectrum	Model *	$N_{\rm H}^{\dagger}$	Index	T (keV)	χ^2/ν	$f_{\rm x}^{\S}$	$L_{\rm x}^{\S}$
all	POWL	8^{+2}_{-1}	$3.2^{+0.3}_{-0.3}$		8.1/5	8.37	29.9
(S/N≧10)	THBR	5^{+1}_{-1}		$0.6^{+1.1}_{-0.1}$	7.2/5	7.54	26.9
	THPL	$0.8^{\rm fix\,\sharp}$		$1.2^{+0.1}_{-0.1}$	59.4/6	5.68	20.3
central	POWL	22^{+23}_{-10}	4^{+2}_{-1}		2.1/3	3.46	12.4
(S/N≧8)	THBR	10^{+9}_{-3}		$0.7^{+0.3}_{-0.2}$	1.8/3	2.71	9.7
	THPL	2^{-1}_{+1}		$1.3^{+0.2}_{-0.1}$	10.8/3	2.21	7.9
clocal	POWL	39^{+49}_{-22}	$4.2^{+2.4}_{-1.5}$		0.08/4	1.86	6.6
(S/N≧6)	THBR	20^{+46}_{-11}		$0.6^{+0.6}_{-0.3}$	0.10/4	1.86	6.6
	THPL	4^{+4}_{-2}		$1.5^{+0.8}_{-0.2}$	3.9/4	1.74	6.2
disk	POWL	16^{+24}_{-6}	$4.0^{+1.6}_{-0.8}$		2.1/4	2.19	7.8
(S/N≧6)	THBR	9^{+8}_{-3}		$0.4^{+0.2}_{-0.1}$	3.2/4	1.98	7.1
	THPL	$0.8^{\rm fix\,\sharp}$		$0.9^{+0.1}_{-0.1}$	19.9/5	1.36	4.7
halo	POWL	8^{+4}_{-3}	$3.9^{+0.7}_{-0.6}$		11.1/3	2.38	8.5
(S/N≧6)	THBR	4^{+2}_{-1}		$0.4^{+0.1}_{-0.1}$	6.1/3	2.14	7.6
	THPL	$0.8^{\rm fix\,\sharp}$		$0.3^{+0.1}_{-0.1}$	10.5/4	1.72	5.8

* POWL: power law, THBR: thermal bremsstrahlung, THPL: thin thermal plasma

† in units of 10^{20} cm^{-2}

§ in units of 10^{-13} erg cm^{-2} s^{-1} and 10^{39} erg s^{-1}, respectively, for 0.1–2.4 keV band, corrected for Galactic absorption and calculation of 1σ errors

♯ fixed to Galactic foreground for spectral fits

thermal plasma model by assuming two temperatures. This is done mostly to compare ours with published results on similar objects, and it is partly justified by the fact that the requirement of a lower-than-galactic absorbing column in the 1-temperature fit could be suggestive of an additional very soft component. Indeed we find best fit values of $\rm kT_1 \sim 0.3 - 0.5$ and $\rm kT_2 \geq 1$ keV, for a the minimum χ^2 reduced to an acceptable value of 5.3 (for 4 degrees of freedom) and the best fit $\rm N_H$ consistent with the Galactic value.

The halo region cannot be fit by any of the simple models ($i.e.$ the minimum χ^2_ν value is larger than 2 in all cases). In spite of the limited significance of our procedure, we have nevertheless tried to fit the data with both a two-component model ($i.e.$ two bremsstrahlung models and a bremsstrahlung and a thin plasma model) and with a thin plasma model with varying abundances. In both cases the minimum χ^2 value reduces drastically to perfectly acceptable values (1.5 and 2.2) and the best fit values are kT 0.2 and 1 keV (2-T model) and kT 0.5 keV, 5% solar abundance. While it is therefore possible that more sophisticated models might be required for this region, given the limited statistical significance of the data, we cannot discriminate between different scenarios, nor can we be sure that our more sophisticated modeling of the data is correct, since we are left with 1 or 2 degrees of freedom. Since the resulting fluxes that we can derive with the different best fit models are all very similar (see Table 7), we will therefore assume the best fit values from the thin thermal plasma model for counts to flux conversion purposes for the halo emission.

3.4. NGC 3079 nuclear X-ray emission

While in the PSPC the nuclear source can not be resolved (see Fig. 5), a complex source is resolved with the HRI resolution at the galaxy's center (Fig. 4) with an extent of the order of $20'' \times 30''$ ($1.7{\rm kpc} \times 2.5$ kpc). In addition, a connected peak at $\sim 25''$ distance north of the nucleus and a separate peak to the SW (source H13) can be clearly seen.

The radial distribution of the emission, centered on the X-ray peak, and its morphology both indicate that the source is extended and structured and that a possible point source located at the nuclear position could only contribute $\sim 1/3$ of the emission in the area. If this source indeed coincides with the active nucleus of the galaxy, its estimated count rate of $\sim 2 \times 10^{-3}$ cts s^{-1} would correspond to a luminosity $\rm L_x > 5 \times 10^{40}$ erg s^{-1}, calculated assuming a thermal bremsstrahlung model with a low energy absorption equivalent to a column density of $\sim 5 \times 10^{20}$ cm^{-2}. The lower limit sign is due to the fact that the absorption in the nucleus is likely to be much higher than the value assumed (which corresponds to an average column density in the disk on NGC 3079, see H I maps (Irwin & Seaquist 1991) and best fit parameters from spectral fits). While a different choice of the spectral model would give very similar values (see Table 7), the low energy absorption adopted influences very strongly the estimate of the intrinsic flux in the ROSAT band. mm-wave estimates of the extinction towards the nucleus of this source indicate that a minimum of 1.4×10^{24} $\rm H_2$ cm^{-2} should be expected (Sofue & Irwin 1992). ASCA data (Serlemitsos et al. 1997; Dahlem et al. 1998) in fact suggest the presence of a hard and heavily absorbed component (with absorbing column in excess of 10^{22} cm^{-2}; however notice that Ptak et al. (1998) give much lower best fit values for absorption to the power law component) in the spectrum of NGC 3079 as a whole (the spatial resolution of ASCA allows only a global measure of the spectral properties of NGC 3079), with a luminosity $\rm L_x$(2-10 keV) of 2×10^{40} erg s^{-1}. The origin of this emission is not as yet unambiguously interpreted, since it is present both in galaxies with recognized nuclear activity (Low luminosity AGN, LINER) and in starburst galaxies (Serlemitsos et al. 1997; Ptak et al. 1998; Dahlem et al. 1998); therefore, due to the lack of good spatial resolution at high energies, it can either be related to the nuclear activity or to the binary population and starburst phenomenon (or both). Given the high absorption suggested by the data and the presence of nuclear activity, in NGC 3079 this component could come from a very absorbed compact nuclear source. In this case we expect about 6×10^{-4} cts s^{-1} in the nucleus with the HRI. Given the large uncertainty (also in absorption) this rate could be consistent with the possible point source contribution from a nuclear source in the HRI image (see above).

Given the strong contamination from the diffuse background, and the small statistics (about 40 cts), we cannot really

Table 8. X-ray parameters for NGC 3073 and MCG 9-17-9

Galaxy		Count rate (10^{-4}s^{-1})	f_X *	L_X **
NGC 3073	PSPC	0.8±0.5	0.9±0.6	0.3±0.2
	HRI	0.3±0.2	1.3±0.9	0.5±0.3
MCG 9-17-9	P9	38± 6	44± 7	15.7±2.5
	H6	8.4±2.2	33± 9	11.8±3.2

* fluxes in units of 10^{-15} erg cm^{-2} s^{-1} for a 5 keV thermal bremsstrahlung spectrum in the 0.1–2.4 keV band, corrected for Galactic absorption

** luminosity in units of 10^{38} erg s^{-1} assuming a distance of 17.3 Mpc

measure possible time variability in the flux from this source, which would confirm its point-source nature and propose an identification with a super-luminous X-ray binary close to the nucleus or the X-ray detection of the NGC 3079 active nucleus itself.

3.5. NGC 3073 and MCG 9-17-9

We searched for X-ray emission from the companion galaxies of NGC 3079, NGC 3073 and MCG 9-17-9. Only MCG 9-17-9 was detected (H6/P9). The 69 counts detected with the PSPC are insufficient for a detailed spectral fitting, and we could only determine one of the two hardness ratios (see Table 4). Comparison with the plots of Fig. 1 indicates that for these two spectral models the source is probably absorbed above the line-of-sight value, and that its spectrum is relatively hard ($i.e.$ kT $>$0.5 keV or $\alpha < 1$).

A weak enhancement is seen at the position of NGC 3073 both in the HRI and in the PSPC, however with a significance far below the threshold for our source catalogs.

Table 8 summarizes PSPC and HRI count rates, X-ray fluxes f_X and luminosity L_X for these sources. To convert count rates to fluxes we assumed a 5 keV thermal bremsstrahlung spectrum (see Table 2); the same distance as for NGC 3079 was assumed for the luminosity determination.

The comparison of the HRI and PSPC flux of MCG 9-17-9 indicates that the source has not varied between the two observations.

4. Discussion

The ROSAT PSPC observations of the edge-on NGC 3079 have shown a complex emission in and outside of the plane of the galaxy. The global X-ray luminosity in the ROSAT band is $\sim 3 \times 10^{40}$ erg s^{-1} (d=17.3 Mpc), higher ($\sim$ factor 10) than what is observed in other edge-on late-type galaxies of similar optical luminosity (for example in NGC 4631, Vogler and Pietsch 1996; NGC 4565, NGC 5907, Vogler et al. 1995). The emission has been separated into three components of similar brightness - disk, central region, and halo - that will be discussed separately in the following subsections.

Two explanations for the enhanced X-ray luminosity of NGC 3079 can be put forward that are triggered by anomalies of the galaxy measured in other wavelength regimes:

1. The galaxy belongs to a group of powerful far infrared emitters, with a far infrared excess comparable to that of starburst galaxies like M82, NGC 253, and NGC 2146 (Lehnert & Heckman 1995). In fact the X-ray, optical and far infrared luminosities of NGC 3079 and NGC 2146 are almost identical (Armus et al. 1995). As we discuss later similarities of the galaxies do not stop there. It is therefore likely that enhanced star formation activity is not only present in the nuclear area but rather widespread in the disk, and therefore it is not remarkable that the X-ray luminosity is also enhanced.
2. On the other hand NGC 3079 harvests a low ionization nuclear emission line region (LINER) or Seyfert 2 type nucleus (Heckman 1980, Ford et al. 1986). In addition, it is known to contain a bright continuum nuclear radio source and bipolar jet like structures emerging from the nucleus along the projected minor axis (extent 50″ see Fig. 11). Similar features and classification of the nucleus also apply for NGC 4258 and M51 and even for the starburst galaxy M82, Tsuru et al. (1997) argue from the analysis of wide-band X-ray spectra for the presence of an obscured low-luminosity AGN. These galaxies were detected as just as bright extended X-ray emitters by ROSAT (e.g. Pietsch et al. 1994, Ehle et al. 1995, Read et al. 1997). This makes it conceivable that jet-like outflows from active nuclei might indicate enhanced extended X-ray emission.

While it is not clear which of these types of activity (or even both?) is responsible for the enhanced X-ray emission, both may have been triggered by galaxy galaxy encounters in the NGC 3079 galaxy group that also contains NGC 3073 and MCG 9-17-9 (see Sect. 4.5).

The low X-ray flux associated with NGC 3079 has not allowed us to properly measure the spectral characteristics of the emission components, therefore a physical interpretation of the results is not possible. As shown in Sect. 3.3.2, a power law model with relatively steep spectral index or a soft thermal bremsstrahlung could fit the data equally well. However, the power law index is in all cases very steep ($\alpha_E \geq 2$) and also the temperature of the thermal bremsstrahlung spectra is rather low if we compare them for instance with spectral fits to individual X-ray binaries or the integral bulge spectrum (primarily X-ray binaries) found with the ROSAT PSPC for M31 (α_E $0.3 - 0.6$ or temperatures above $\sim$ 1 keV, Supper et al. 1997). It is likely that the simple models that we have assumed here for lack of statistics are inadequate to represent the more complex characteristics of the X-ray emission in these objects (for example a population of individual sources plus a multitemperature or non-equilibrium interstellar medium). Dahlem et al. (1998) have shown that a correct interpretation of the spectra of galaxies requires data in a larger energy range than provided by the PSPC data alone, even though there are still residual ambiguities in the correct model to be used. In particular they find in several

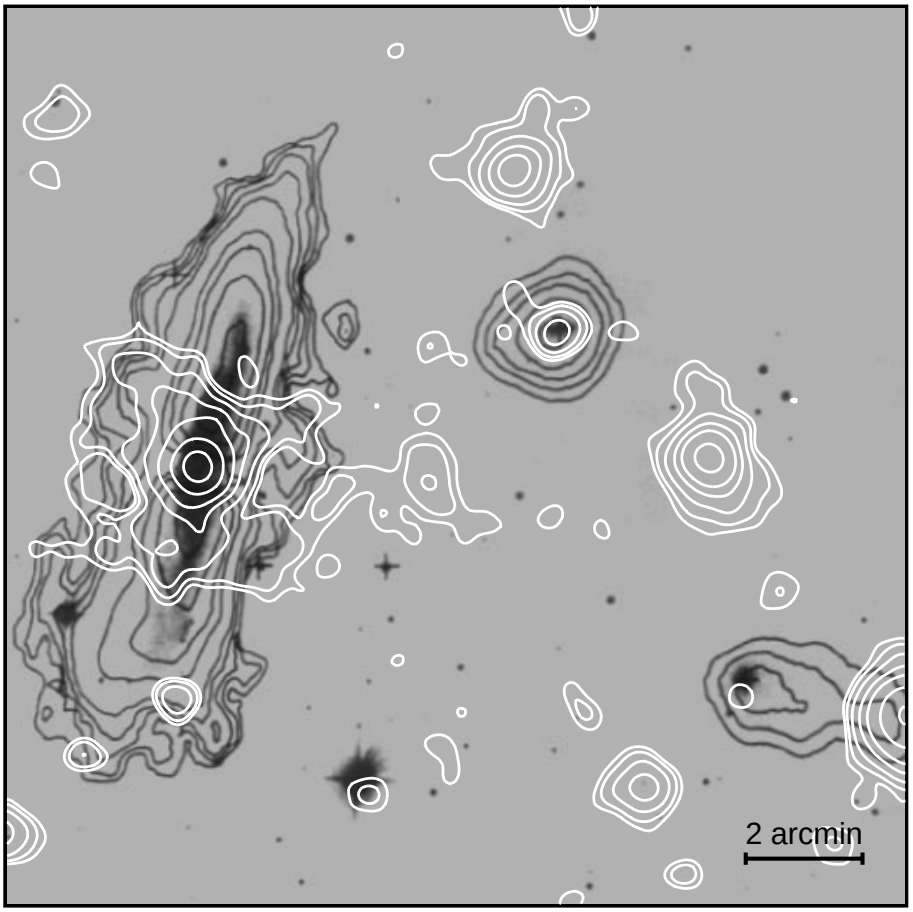

Fig. 10. Contour plot of the broad band PSPC X-ray emission of the region of NGC 3079 and its companions overlaid in white on Fig. 1 of Irwin et al. 1987, showing H I-contours in black superposed on an reproduction of the POSS red plate. The same contour levels as in Fig. 3 are used

instances that two gas phases are needed in addition to a power law component at high energies. The lack of spatial resolution however does not allow a proper investigation of the location of these individual components, that cannot therefore be unambiguously identified with the separate sources of emission in galaxies. In this respect, only future X-ray missions, that combine high sensitivity with good spectral and spatial resolution over a large energy range will allow a significant step forward in our understanding of the X-ray properties of galaxies. From the present data however we could be tempted to assume that indeed a multiphase interstellar medium is present and interpret the (very crude) indication of the hardness ratios in terms of temperature variations in the disk versus central region, and assign a higher temperature to the emission coming from the central source coincident with the super-bubble (see Sect. 4.2). This would be analogous to the results from the more detailed analysis of NGC 253, for which the central starbursting region is harder than the surrounding disk (Dahlem et al. 1998).

In either case however a large low energy absorption is suggested, well above the line-of-sight H I column density. This result is not surprising since the disk is embedded in an extended H I disk (Irwin et al. 1987). Only at large distances from the plane could local obscuration be neglected, and indeed the (though extremely uncertain) results for the halo region do not require large absorbing columns.

4.1. X-ray emission from the disk of NGC 3079

Several bright sources are detected in the galaxy plane of NGC 3079 (Table 5), with luminosities higher than 10^{38} erg s^{-1}, $i.e.$ well above the Eddington luminosity for a 1 $M_\odot$ accreting object. As already discussed, these could be real point-like sources or could be local enhancements in a more diffuse emission. However, the optical image of the galaxy shows a very patchy appearance, and there are a lot of giant H II regions in the plane (Veilleux et al. 1995). Over-luminous H II regions, relative to those observed in our galaxy and in other normal spirals like M101, for which $L_x \leq 10^{38}$ erg s^{-1} (Williams & Chu 1995), have already been observed in relation with the presence of enhanced star formation ($e.g.$ in the Antennae, Read et al. 1995, Fabbiano et al. 1997). As discussed above, the integral spectrum of the disk region is rather soft compared to bright X-ray binary spectra and can be taken to favor the over-luminous H II region origin of the emission. Deep observations with improved spatial and spectral resolution are needed to solve the origin of the disk emission.

4.2. X-ray emission from nuclear super-bubble of NGC 3079

NGC 3079 hosts the most powerful example of a wind-blown bubble to the east of its nucleus. Recent spectroscopic studies in the near infrared and optical however argue against a star-

burst origin for the powering of the wind, and suggest an active nucleus with somewhat exceptional properties (Hawarden et al. 1995). In this case, one would expect a wind from an active galactic nucleus (AGN, see Heckman et al. 1986) – how can X-ray observations help understanding the nature of this source?

Emission in the center of NGC 3079, coincident with the Hα loop (Ford et al. 1986) and the kiloparsec scale radio lobes (de Bruyn 1977, Duric & Seaquist 1988) is clearly detected in the HRI data. The source appears complex (see Fig. 11). A possible unresolved component, apparently shifted by about 3″ to the east from the position of the optical nucleus (marked by the cross in Fig. 11) could be – within the systematic position errors – coincident with the nucleus. This source, if identified with the hard spectral component measured by ASCA (see discussion in Sect. 3.4) that has been associated with the emission of an highly absorbed AGN, is brighter by a factor of 3 – 4 than the extrapolation of the ASCA spectrum into the ROSAT band would suggest. If the positional displacement however is real, it could represent the brightest and hottest part of the out-flowing material that is not shielded by the absorbing material in the central disk. Such a displacement to the east is expected in such a scenario due to the high absorption in the inner disk of NGC 3079 and the disk orientation. The inclination of 84° and the orientation of the galaxy (the western side of the disk is closer to us than the eastern side) lead to reduced absorption in the direction to the nuclear area in the east and high absorption in the west (N_H in the inner disk is $> 10^{22}$ cm^{-2} according to Irwin & Seaquist 1991). The high absorption may also cause that no X-ray or Hα emission coinciding with the western component of the radio jet is detected.

A more extended component elongated to the north is possibly connected to a feature seen at larger scale (Fig. 11), and may indicate a preferred channel to fuel the emission in the halo.

The HRI attitude solution carefully derived in Sect. 2.1 clearly contradicts the solution put forward by Dahlem et al. (1998) which is shifted to the north by 15″ and – if correct – would exclude a connection of the central X-ray emission with either the nucleus or the nuclear super-bubble of NGC 3079.

The small extension of the bright central X-ray emission region compared to the PSPC spatial resolution coupled with it's low flux prevents us from reliably determining spectral properties. In the innermost 30″ radius, that correspond to the minimum cell size for count extraction that is reasonable for PSPC data, the HRI resolution indicates that at least three different components are present, all contributing to the overall emission: the disk with two non nuclear point-like sources, the nuclear bubble and the unresolved point source. Neither of these dominates, with the possible exception of the disk emission, which can in part be subtracted by choosing a local background (see Table 6), and therefore a spectral analysis should take all of them into account. This is clearly unrealistic given the small number of photons that can be collected in the area and also given the limited spectral capabilities of the PSPC, that indeed indicate a single model as acceptable. Whether one can however use the results of any such fit and interpret them as giving a physical interpretation of the observations remains questionable. Observations with better statistics and higher spectral and spatial resolution and an extension to higher energies are needed badly. Only then will we be able to answer the question if the – with ROSAT HRI – unresolved component 3″ to the east of the optical nucleus is coincident with the optical nucleus and the hard ASCA source (see above) or – our prefered explanation – the brightest and hottest part of the out-flowing material.

We can compare the emission from the nuclear super-bubble to the X-ray emission from the plume detected in NGC 253 (see Pietsch et al. 1998), the anomalous arms of NGC 4258 (see Pietsch et al. 1994), and the extended emission resolved with the HRI in NGC 2146 (Armus et al. 1995), X-ray features of similar appearance and proposed origin. While in the prototypical starburst galaxy NGC 253 the plume has an extent perpendicular to the major axis of ~ 700 pc and a luminosity of 2×10^{39} erg s^{-1}, in the LINER galaxy NGC 4258 the extent is 1.5 kpc and the luminosity is 5×10^{39} erg s^{-1}. For the starburst galaxy NGC 2146 (after correcting for an inclination of 36°, Tully (1988)) the HRI extent is 2.2 kpc and the unresolved luminosity in the range of 5×10^{39} erg s^{-1}. Due to the low inclination of NGC 2146, however, it is not possible to determine the scale height of the extended emission perpendicular to the galaxy disk and separate point-like and extended components. In comparison the NGC 3079 central component has an extent of 1.7 kpc and a luminosity of 7×10^{39} erg s^{-1}. NGC 253 and NGC 2146 show coinciding optical line emission, that is explained by an out-flowing wind driven by the nuclear starburst. Close to the nucleus of NGC 253 embedded in the plume emission a slightly extended source represents the hottest part of the out-flowing material and may reflect the point-like nuclear component in NGC 3079. The extended nuclear features in NGC 3079 and NGC 4258 are more X-ray luminous than in the pure starburst galaxies NGC 253 and NGC 2146 and are not only traced by optical emission lines but in addition by jet-like continuum radio emission indicating the importance of magnetic fields funneling the outflow and the existence of a driving AGN.

4.3. Extended X-ray halo of NGC 3079

The PSPC contour plots (Figs. 3 and 10) and the radial distribution of the PSPC and HRI detected photons (Fig. 6) clearly indicate that the emission from NGC 3079 extends to a radius of 13.5 kpc. The distributions along the major and minor axis (Fig. 7) demonstrate that this emission is not only originating within the NGC 3079 disk but is filling the halo to at least the inclination corrected D_{25} diameter of the galaxy. The spectral investigations clarified that the halo emission contributes about one third to the total X-ray luminosity ($\sim 2.7 \times 10^{40}$erg s^{-1}) of the galaxy in the 0.1 – 2.4 keV ROSAT band; emission from the center and the disk complete the luminosity in about equal parts.

The extent of the halo of NGC 3079 is comparable or slightly bigger than the one of the starburst galaxy NGC 253 (Pietsch et al. 1996, 1998) and bigger by a factor of ~ 4 than that of the active galaxy NGC 4258. On the other hand, the luminosities (and temperatures) for the halos are similar in the two galax-

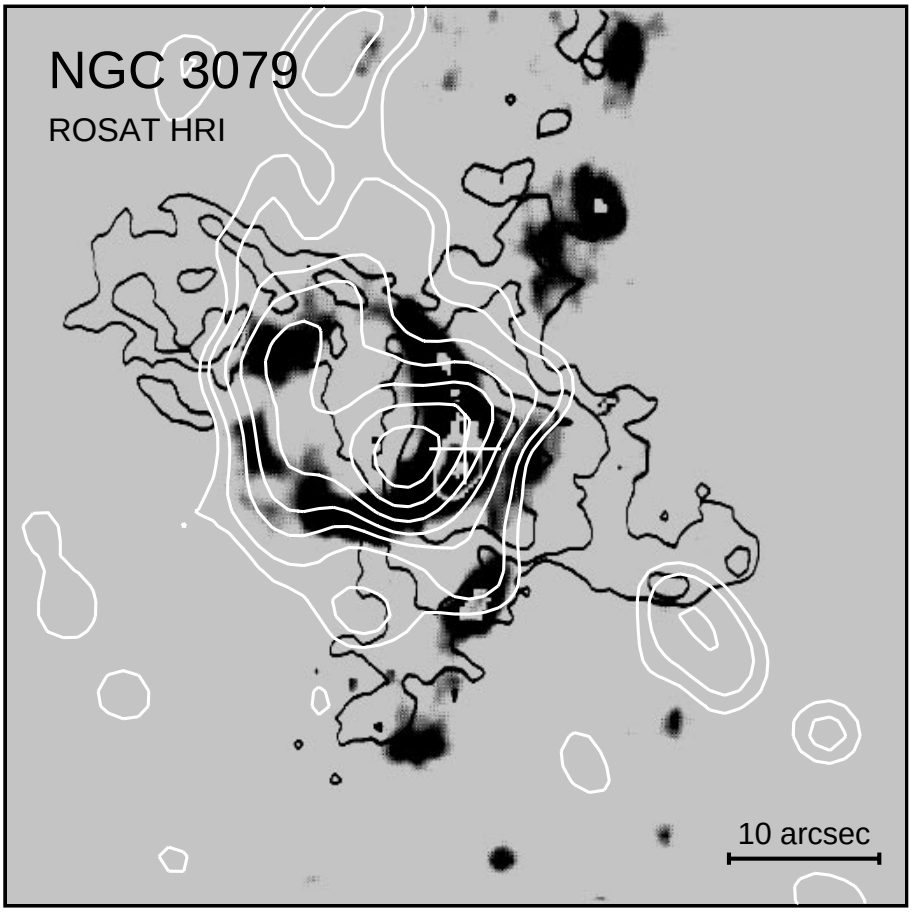

Fig. 11. Contour plot of the central emission region of NGC 3079 for ROSAT HRI overlaid on Fig. 1 of Veilleux et al. (1994), showing the continuum-subtracted distribution of H_α + [N II $\lambda\lambda$6548, 6583 line emission (grey-scale) and the 20 cm continuum distribution (black contours). X-ray contours are given in white (same levels used as in Fig. 4)

ies with known active nuclei,while they are higher than in the starburst galaxy. The halo emission has a X-shaped structure (c.f. Figs. 8 and 10) similar to NGC 253 (however not as clearly resolved due to the greater distance of NGC 3079). X-shaped filaments of the diffuse ionized medium within a radius of 5 kpc, emerging from the inner disk and rising more than 4 kpc above the disk plane of NGC 3079, have been reported from optical [N II] measurements (Heckman et al. 1990, Veilleux et al. 1995). According to Veilleux et al., the morphology, kinematics, and excitation of the filaments suggests that they form a biconic interface between the undisturbed disk gas, and gas entrained in a wide-angle outflow. In H I observations of NGC 3079 numerous arcs and filaments are present extending away from the plane of the edge-on galaxy which seem to be unrelated to the nuclear activity (Irwin & Seaquist 1990). They may indicate gas flow between disk and halo in addition to violent outflow from the active nucleus (Heckman et al. 1990, Filippenko & Sargent 1992).

If we assume that the halo X-ray emission is due to hot gas with a temperature of 3.5×10^6K (cooling coefficient according to Raymond et al. (1976) of 5.5×10^{-23}erg cm^3 s^{-1}), a luminosity of 5.8×10^{39}erg s^{-1}(see Table 7) distributed in a sphere of 13.5 kpc radius with filling factor η we can calculate parameters of the plasma using the model of thermal cooling and ionization equilibrium of Nulsen et al. (1984). The electron densities, masses, and cooling times of the X-ray emitting gas in the halo are: $n_e = 7 \times 10^{-4} \times \eta^{-0.5}$ cm^{-3}, $M_{gas} = 2.0 \times 10^8 \times \eta^{0.5}$ M$_\odot$, $\tau = 1.5 \times 10^9 \times \eta^{0.5}$ yr.

These gas parameters differ significantly from the parameters derived by Read et al. (1997) for NGC 3079 which only use a strongly simplified geometrical model attributing the X-ray emission to a nuclear point source and just one diffuse extended emission component. They find a luminosity that is higher by a factor of ~ 5 and nearly twice the temperature compared to the halo parameters as given in Table 7; *i.e.* their values mix up halo and disk, leading to higher electron densities and gas masses, and slightly longer cooling times. Read et al. analyzed several nearby spiral galaxies using similar simplified models. The resulting parameters for the diffuse gas always overestimate a possible halo component preventing a sensible comparison to the NGC 3079 halo results.

As mentioned above to derive the gas parameters we assumed a spherical distribution with constant temperature. This approximation however, only describes the situation to first order. At least two further details indicated by the ROSAT data should be addressed:

- There is a clear E – W asymmetry (c.f. Fig. 7) and an indication of a X-shape azimuthal distribution in the PSPC broad band counts that will be further discussed below.
- The PSPC contour plots of the S band emission of NGC 3079 show far more azimuthal structure than the more spherically

distributed H1 band emission. This indicates local variations of the halo X-ray spectrum indicative of either changing foreground or intrinsic (within the halo of NGC 3079) absorption and/or temperature variations within the halo gas.

To better understand and characterize these effects spatially resolved spectra are strongly needed which, due to the low counting statistics, can not be tackled with the ROSAT data at present. Temperature profiles of the diffuse emission will help to solve the question of whether the E – W asymmetry can be attributed to inhomogeneities in the galaxy halo or instead it reflects a hot medium connected to the potential of the NGC 3079 group (or both components could be present). This question is also relevant when interpreting H I data of the companion galaxy NGC 3073 which exhibit an elongated tail aligned with the nucleus of NGC 3079; an explanation of the tail due to ram pressure stripping by out-flowing gas from NGC 3079 has been put forward in favor of stripping by movement in an intergroup medium (Irwin et al. 1987). A galactic wind perpendicular to the disk in the general direction of the minor axis can explain the X-shaped halo structure of the X-ray and optical [N II] data (see above).

4.4. NGC 3079 as LINER/Seyfert 2 galaxy

The unified model for active nuclei (Antonucci 1993) has been proposed to explain the properties of the different types of AGN. In this scheme the difference between Seyfert 1 and 2 galaxies is determined by the viewing angle to the nucleus that is embedded in a torus of molecular material. Type 1 Seyfert galaxies allow direct observation of the nucleus, whereas for type 2 galaxies nuclear X-ray emission can only be seen via reflection above or below the torus or dust gains, or via transmission through this torus. X-ray spectra of the nuclear emission are directly probing the absorption depth under which an AGN is seen, and therefore are an important test for the unified scheme.

As discussed in Sects. 3.4 and 4.2, only very little direct emission from the LINER/Seyfert 2 type nucleus of NGC 3079 – if any at all – is detected in the ROSAT band. Due to the many different equally bright components that contribute to the overall X-ray spectrum of NGC 3079 and due to limited counting statistics, integral spectra of the galaxy as obtained by ASCA can not fully separate the nuclear emission component and only give an indication of a highly absorbed power law component that could be related to the nucleus. X-ray spectroscopy with high spatial resolution as expected from the next generation of X-ray observatories (AXAF, XMM) will resolve the ambiguity. From mm-wave estimates of the extinction to the nucleus of NGC 3079 (Sofue & Irwin 1992) and by comparison with integral broad band X-ray spectra of other Seyfert 2 galaxies obtained with the ASCA or BeppoSAX satellites (see Maiolino et al. 1998 and references therein) one may infer absorption depths well in excess of 10^{24} cm^{-2} also for NGC 3079.

Soft X-ray emission in excess of the high energy spectrum has been discovered in many Seyfert 2 galaxies. In Seyfert 1 galaxies such a component may not be observed because it is covered by the bright low absorbed flat power law spectrum. In the nearby Seyfert 2 galaxies NGC 4258 and NGC 1068 the soft component could be resolved and is attributed to emission from a bipolar jet and from the halo of the galaxies (see Pietsch et al. 1994, Wilson et al. 1992). As reported above NGC 3079 show the same components. Therefore, a luminous X-ray halo gas heated by and ejected via jets from the nucleus may not only explain the spatially unresolved soft X-ray emission components reported in other Seyfert 2 galaxies but also be expected in many Seyfert galaxies and AGN.

4.5. Companion galaxies NGC 3073 and MCG 9-17-9

NGC 3079 (total galaxian mass 1.2×10^{11} M$_\odot$) is the dominant galaxy in a group containing NGC 3073 (1.1×10^9 M$_\odot$) and MCG 9-17-9 (3.9×10^9 M$_\odot$)(Irwin et al. 1987). While little is known from observations at other wavelength on MCG 9-17-9 – it's redshift and H I contours may even suggest that it is not physically associated with NGC 3079 – NGC 3073 is discussed as a starburst galaxy situated along the trajectory of the outflow of NGC 3079 with the starburst induced by the super-wind (Filippenko & Sargent 1992).

As shown in Sect. 3.5, MCG 9-17-9 is bright in X-rays with a luminosity of $\sim 1.5 \times 10^{39}$erg s^{-1}while NGC 3073 is barely detected ($< 10^{38}$erg s^{-1}). The luminosity of MCG 9-17-9 is rather high for such a dwarf galaxy (c.f. Markert & Donahue 1985) and may indicate the presence of at least one super-luminous source. Such a source could be a low luminosity active nucleus, a X-ray binary radiating at super-Eddington luminosity, a young supernova or a combination of the above. An alternative explanation could be the existence of several X-ray binary sources radiating close to the Eddington limit for a one M$_\odot$ star. A similarly high luminosity has been reported for the nearby Magellanic-type star forming galaxy NGC 4449 (Vogler & Pietsch 1997). There the emission could be resolved in seven point-like sources and an additional diffuse component of about equal luminosity. The upper limit to the luminosity of NGC 3073 is within the values expected for a galaxy of this mass. The starburst activity of the galaxy does not reflect in it's X-ray luminosity.

5. Summary

We have reported the results of the first detailed analysis of ROSAT data of the NGC 3079 field. We have paid special emphasis on the best attitude solution to achieve optimal HRI point spread function and positional accuracy. With HRI and PSPC we detected 23 and 34 sources within 35′ diameter and a box of 35′×35′, respectively, apart from complex emission from the inner 5′ around NGC 3079. We have identified possible counterparts for several of the sources outside NGC 3079 by comparison with optical plates and catalogues.

The LINER/Seyfert 2 galaxy NGC 3079 manifests itself as a complex X-ray source with a luminosity of 3×10^{40}erg s^{-1} and could be resolved into three components:

(1) Extended emission in the inner 20″×30″ with a luminosity of 1×10^{40}erg s^{-1}can be resolved with the HRI and is coincident with the super-bubble seen in optical images. The active nucleus may contribute to the emission as a point source. We,

however, prefer an explanation of this emission as the brightest and hottest part of the out-flowing material similar to the slightly extended emission emission close to the galaxy nucleus within the plume of NGC 253 (Pietsch et al. 1998).

(2) Emission from the disk of the galaxy has a luminosity of 7×10^{39}erg s^{-1}and can be partly resolved by the HRI in 3 point sources with luminosities of $\sim 6 \times 10^{38}$erg s^{-1}each. The soft spectrum of the disk can be explained by a mixture of X-ray binaries and over-luminous H II regions.

(3) Emission from the halo has a luminosity of 6×10^{39}erg s^{-1}and is rather soft (temperature of 0.3 keV). It extends to nuclear distances of more than 13 kpc and has a X-shaped appearance. Using simplifying assumptions we derived parameters for this halo gas.

The X-ray luminosity of NGC 3079 is higher by a factor of 10 compared to other galaxies of similar optical luminosity. It also exceeds the luminosity seen in starburst galaxies like NGC 253. We argue that this may be caused by the presence of an AGN in NGC 3079 rather then by starburst activity. Investigations of the other galaxies in the NGC 3079 group, NGC 3073 and MCG 9-17-9, showed that the X-ray emission is not extraordinary for their type as might have been expected from the disturbance by the galactic super-wind emanating from the active companion NGC 3079.

Acknowledgements. This research has made use of the SIMBAD database operated at CDS, Strasbourg, France and of the NASA/IPAC Extragalactic Database (NED) which is operated by the Jet Propulsion Laboratory, CALTECH, under contract with the National Aeronautics and Space Administration. To overlay the X-ray data we used an image based on photographic data of the National Geographic Society – Palomar Observatory Sky Survey (NGS-POSS) obtained using the Oschin Telescope on Palomar Mountain. The NGS-POSS was funded by a grant from the National Geographic Society to the California Institute of Technology. The plates were processed into the present compressed digital form with their permission. The Digitized Sky Survey was produced at the Space Telescope Science Institute under US Government grant NAG W-2166. GT acknowledges a Max-Planck Fellowship and the kind hospitality of the ROSAT group during the completion of this project. The ROSAT project is supported by the German Bundesministerium für Bildung, Wissenschaft, Forschung und Technologie (BMBF/DLR) and the Max-Planck-Gesellschaft (MPG).

Appendix A: Sources in the field of NGC 3079

A.1. Correlation of HRI and PSPC detections

Thirty-four sources are detected around NGC 3079 in the PSPC and HRI observations. Table A1 shows their characteristics. If the source has only been detected in one of the detectors, a 2σ upper limit at the source position has been determined for the other detector. No upper limit is computed for sources detected in the PSPC that are at a large off-axis angle in the HRI, since we cannot reliably measure the count rates (the effective exposure time could be lowered as a consequence of the wobbling motion that can place the source outside the field of view for part of the observation, the detector sensitivity and the PSF are poorly known). We checked the mean offset of the source positions (listed in col. 3 of Table A1 for those sources detected in both instruments) to verify our attitude solution of Sect. 2.3 for all sources. The mean offsets in the north-south and east-west directions were below the systematical error.

The distribution of the hardness ratios listed in Table 4 is shown in Fig. 1. Comparison with the theoretical values calculated for power law and thermal bremsstrahlung spectra (Fig. 1) show that in most cases the sources have hardness ratios consistent with a moderate amount of absorption, as expected from the line-of-sight Galactic H I column density value.

For several sources the derived fluxes or upper limits were comparable in the two separate observations. For four sources detected in both observations, namely H1/P3, H5/P7, H8/P10, and H9/P12 the flux differences exceed 2σ. For one additional source detected only in one of the observations, namely P17, the 2σ HRI upper limit is lower by more than twice the error on the corresponding detection. Since the expected uncertainty in the count to flux conversion factor is of the order of 15% at most (see Sect. 2), the assumption of a wrong spectral model should not cause these flux differences. However, it should be noted that two of these sources, H1/P3 and H5/P7, are at large off-axis angles, so possible effects due to their positioning in the detector might come into play. We have checked for example the position of source H5 in detector coordinates, to understand whether the wobbling motion could affect the effective exposure of this source, and found that it is in fact possible that the source falls outside of the detector field of view for part of the observation, so the flux quoted should in fact be considered a lower limit. The same consideration does not apply to the other sources and it is therefore likely that these sources have varied between the two observations. As discussed in the next section, four of the variable sources are coincident in position with stellar objects or active nuclei (see Table A1), which as a class are known to be variable sources, and would therefore support the idea that the observed variations are real: H5/P7 is identified with QSO 0957+5543 at a redshift z=2.1, H9/P12 with the well studied QSO 0957+5608AB, a double source originating from a quasar at z=1.4 that is gravitationally lensed by a cluster of galaxies at z=0.4.

A.2. Identification of X-ray sources in the field of NGC 3079

For each source detected we prepared APM finding charts (Irwin et al. 1994), from which we can get a positional accuracy for the optical candidates of better than $2''$, optical magnitudes in blue (O) and red (E), and the color index O-E. In the charts sources are classified as stellar, non-stellar, or blend. Optical counterparts were searched for each in a circle of the X-ray position error.

Several positional coincidences were found from these charts. Additional candidates resulted from correlations of our source catalog with the entries in the SIMBAD and NED databases and with radio sources in the field given in Irwin and Seaquist (1991).

To improve on the reliability of the identifications, we have estimated the $\log(f_x/f_v) = \log(f_x) + (m_v/2.5) + 5.37$ (see Maccacaro et al. 1988), that we can use to discriminate between

Table A1. X-ray properties of the sources in the NGC 3079 field and proposed identifications

ROSAT name (RX J) (1)	Source no. (2)	Δ (″) (3)	HRI flux * (4)	PSPC flux * (5)	Identification (6)	Δ (″) (7)	$\log(\frac{f_x}{f_v})$ (8)	Ref. Notes (9)
095956.3+554639	P1			5.2±0.9	APM O681 stellar (14.9, 0.5)	17	−2.2	1,6
100008.8+553448	P2			4.2±0.9				6
100032.3+553631	H1/P3	2.1	33.5±3.0	43.2±1.9	APM O681 (18.0, 0.6)	4	−0.1	1
100037.4+555046	P4		<12	3.1±0.8	APM 1331 stellar (20.0, 0.3)	6	−0.2	1
100056.4+553519	H2/P5	3.0	17.6±2.0	19.4±1.3	APM O681 stellar (19.6, 0.6)	2	0.3	1
					radio source	5		2
100058.9+555141	H3		3.8±1.1	<2.3	APM 1331 (20.5, 2.4)	6	−0.8	1
100104.7+553519	H4/P6	3.0	3.6±1.1	5.3±0.8	APM O681 stellar (18.9, 0.7)	6	−0.6	1
					Q0957+5549 z=1.5	4		3,5
100110.0+552838	H5/P7	11.4	(>9.4±2.0)	19.7±1.4	APM 1331 stellar (16.9, 0.3)	5	−0.7	1,6
					Q0957+5543 z=2.1	4		3,5
100113.3+554906	P8		<0.7	3.7±0.9				
100114.6+554310	H6/P9	0.7	3.3±0.9	4.4±0.7	APM 1331 (8.9, 1.3)	7	−5.0	1
					MCG 9-17-9	7		2
100116.8+554709	H7		2.1±0.8	<2.1				
100119.7+554559	H8/P10	5.3	5.0±1.1	10.0±1.0	APM 1331 stellar (21.7, <1.7)	1	>0.4	1
100120.9+553244	P11		<2.8	1.9±0.6				
100120.6+555355	H9/P12	6.3	146.1±5.6	200.8±3.8	APM 1331 (14.3, 0.1),	4	−0.6	1
					lensed Q0957+5608AB z=1.4	3		2,5
100123.5+553953	H10		1.7±0.7	<1.6				
100130.2+554033	P13		<0.5	3.6±0.9				
100138.2+553508	H11		2.3±0.8	<2.3	HD 86661 (8.7, 0.7) G8IV-V**	1	−5.1	4
100146.6+555036	P14		<1.6	2.2±0.6				
100156.3+555434	P15		<2.2	4.2±0.8	APM 1331 stellar (18.7, 0.9)	4	−0.9	1
100200.5+553200	P17		<1.9	7.4±0.9	APM 1331 stellar (20.8, 0.9)	10	0.2	1
100205.0+554555	H17		1.5±0.6	<5.3				
100206.2+552750	P20		<1.6	1.2±0.6				
100223.0+553429	H19/P22	9.0	6.7±1.3	5.7±0.8	HD 237859 (10.6, 1.1) F0	2	−4.0	4
100228.2+553941	P23		<0.3	2.4±0.7				
100237.4+553505	P24		<3.7	2.0±0.6	APM 1331 stellar (19.7, 3.7)	13	−1.9	1
100240.8+552750	P25		<1.6	2.8±0.7	APM 1331 (21.7, 3.1)	14	−0.7	1
100245.5+554648	H20/P26	5.8	6.2±1.2	4.3±0.7	APM 1331 stellar (21.8, <1.8)	4	>0.0	1
100244.9+555110	P27		<1.2	2.2±0.7	radio source	13		2
100245.1+555758	P28			17.3±1.5				6
100254.2+554226	H21		2.3±0.8	<1.3				
100303.4+554752	H22/P29	5.5	3.9±1.1	3.0±0.7	APM 1331 stellar (12.2, 0.9)	3	−3.6	1,6
100305.5+553727	P30		<1.5	1.6±0.6				
100309.6+554135	H23/P31	5.2	14.6±1.9	14.6±1.2	APM 1331 stellar (19.1, 0.5)	1	0.0	1
100327.8+552625	P32		***	3.7±0.9	APM 1331 stellar (20.4, 0.9)	9	−0.2	1
100333.5+553627	P33		<8	5.4±0.9				
100343.6+553331	P34			4.9±0.9				6

* fluxes or 2σ upper limits in units of 10^{-14} erg cm^{-2} s^{-1} for a 5 keV thermal bremsstrahlung spectrum in the 0.1–2.4 keV band, corrected for Galactic absorption

** The optical position has been corrected for proper motion

*** outside HRI field of view

References and Notes: (1) Irwin et al. 1994; (2) Irwin & Seaquist 1991; (3) Bowen et al. 1994; (4) SIMBAD; (5) NED; (6) source at an off-axis angle $\geq 15'$ In the HRI detector. No upper limit is calculated for these sources (see text)

stars, for which $\log(f_x/f_v)$ is generally < -1, and AGN for which this quantity is in the range -1.2 to +1.2 (see also Brinkmann 1992 and Pflüger et al. 1996). X-ray fluxes in the 0.1–2.4 keV band have been determined from the count rates assuming a 5 keV thermal bremsstrahlung spectrum, corrected for Galactic absorption (see Table 2). For the optical magnitude we used the 'E' magnitude from the APM catalog.

Proposed identifications for 21 of the ROSAT field sources are summarized in Table A1. Column 6 lists the APM field and classification, and in parenthesis the O luminosity and the color

(O–E). The optical identification and the spectral type given for stars are taken from the SIMBAD database. Identifications for extragalactic objects, with their redshift when available, is based on the NED database. The separation to the X-ray position is given in col. 7. $\log(f_x/f_v)$ and references used are indicated in cols. 8 and 9.

In most cases there is only one APM candidate within the error radius of the X-ray source. All proposed identifications are located within the X-ray position errors. Three sources are identified with known QSOs (H4/P6, H5/P7, H9/P12). Two sources (H2/P5 and P27) are identified with radio sources, for the first of the two there is also a APM candidate. Two sources (H11 and (H19/P22)) are identified with stars cataloged in SIMBAD.

The $\log(f_x/f_v)$ values and the optical colors of the unidentified objects show values similar to those of the identified QSOs. This suggest that most of them are also AGN/QSOs.

$\log(f_x/f_v) < -1$ are seen in only three unidentified sources, P1, P24 and H22/P29, for which identifications with stars are suggested. The optical candidates of H3, P25, and P24 show rather red colors. The candidates for H3 and P25 are flagged by APM as non-stellar in the red and stellar in the blue. It is likely that an AGN embedded in a host galaxy is the optical counterpart of these sources.

References

Antonucci R.R.J., 1993, ARA&A 31, 473
Armus L., Heckman T.M., Weaver K.A., Lehnert M.D., 1995, ApJ 445, 666
Aschenbach B., 1988, Appl. Opt. 27, 1404
Baan W.A., Irwin J.A., 1995, ApJ 446, 602
Bowen D.V., Osmer S.J., Blades J.C., et al. , 1994, AJ 107, 461
Braine J., Guélin M., Dumke M., et al., 1997, A&A 326, 963
Brinkmann W., 1992, First Results from the ROSAT Survey. In: Duschl W.J., Wagner S.J. (eds.) Physics of Active Galactic Nuclei. Springer Verlag, Berlin, p. 19
Cruddace R.G., Hasinger G.R., Schmitt J.H.M.M., 1988, In: Murtagh F., Heck A. (eds.) Astronomy from large databases. ESO Conference and Workshop Proc. 28, p. 177
Dahlem M., Weaver K.A., Heckman T.M., 1998, ApJS, accepted
de Bruyn A.G., 1977, A&A 58, 221
Dickey J.M., Lockman F.J., 1990, ARA&A 28, 215
Duric N., Seaquist E.R., 1988, ApJ 326, 574
Duric N., Seaquist E.R., Crane P.C., Bignell R.C., Davis L.E., 1983, ApJ 273, L11
Ehle M., Pietsch W., Beck R., 1995, A&A 295, 289
Fabbiano G., Feigelson E., Zamorani G., 1982, ApJ 256, 397
Fabbiano G., Kim G.-W., Trinchieri G., 1992, ApJS 80, 531
Fabbiano G., Schweizer F., Mackie G., 1997, ApJ 478, 542
Filippenko A.V., Sargent W.L.W., 1992, AJ 103, 28
Ford H.C., Dahari O., Jakoby G.H., Crane P.C., Ciardullo R., 1986, ApJ 311, L7
Gallimore J.F., Baum S.A., O'Dea C.P., Brinks E., Pedlar A., 1994, ApJ 422, L13
Greenhill L.J., Jiang D.R., Moran J.M., et al., 1995, ApJ 440, 619
Hawarden T.G., Israel F.P., Geballe T.R., Wade R., 1995, MNRAS 276, 1197
Heckman T.M., 1980, A&A 87, 152
Heckman T.M., 1986, PASP 98, 159
Heckman T.M., Armus L., Miley G.K., 1990, ApJS 74, 833
Henkel C., Güsten R., Downes D., et al., 1984, A&A 141, L1
Hummel E., van Gorkom J.H., Kotanyi C.G., 1983, ApJ 267, L5
Irwin J.A., Seaquist E.R., 1990, ApJ 353, 469
Irwin J.A., Seaquist E.R., 1991, ApJ 371, 110
Irwin J.A., Sofue Y., 1992, ApJ 396, L75
Irwin J.A., Seaquist E.R., Taylor A.R., Duric N., 1987, ApJ 313, L91
Irwin M., Maddox S., McMahon R., 1994, Spectrum 2, 14
Kim D.-W., Fabbiano G., 1995, ApJ 441, 182.
Lehnert M.D., Heckman T.M., 1995, ApJS 97, 89
Maccacaro T., Gioia I.M., Wolter A., Zamorani G., Stocke J.T., 1988, ApJ 326, 680
Maiolino R., Salvati M., Bassani L., et al., 1998, A&A, accepted
Markert T.H., Donahue M.E., 1985, ApJ 297, 567
Nulsen P.E.J., Stewart G.C., Fabian A.C., 1984, MNRAS 208, 185
Pfeffermann E., Briel U.G., Hippmann H., et al., 1988, Proc. SPIE 733, 519
Pflüger B., Otterbein K., Staubert R., 1996, A&A 305, 699
Pietsch W., Vogler A., Kahabka P., Jain A., Klein U., 1994, A&A 284, 386
Pietsch W., Supper R., Vogler A., 1996, In: D. Kunth et al. (eds.) The interplay between massive stare formation, the ISM and galaxy evolution. Editions Frontieres, Gif-sur-Yvette Cedex, France, p. 179
Pietsch W., et al., 1998, A&A, in preparation
Ptak A., Serlemitsos P., Yaqoob T., Mushotzky R., 1999, ApJS, in press (ASTROPH-9809159)
Raymond J.C., Cox D.P., Smith B.W., 1976, ApJ 204, 290
Read A.M., Ponman T.J., Wolstencroft R.D., 1995, MNRAS 277, 397
Read A.M., Ponman T.J., Strickland D.K., 1997, MNRAS 286, 626
Reichert G.A., Mushotzky R.F., Filippenko A.V., 1994, In: I. Shlosman (ed.) Mass-Transfer Induced Activity in Galaxies. Cambridge University Press, Cambridge, UK, p. 302
Seaquist E.R., Davies L., Bignell R.C., 1978, A&A 63, 199
Serlemitsos P., Ptak A., Yaqoob T., 1996, In: Eracleous M., Koratkar A., Leitherer C., Ho L. (eds.) The Physics of LINERs in View of Recent Observations. 70
Snowden S., McCammon D., Burrows D., Mendenhall J., 1994, ApJ 424, 714
Soifer B.T., Boehmer L., Neugebauer G., 1989, AJ 98, 766
Supper R., Hasinger G., Pietsch W., et al., 1997, A&A 317, 328
Trinchieri G., Kim D-W., Fabbiano G., Canizares C.R.C., 1994, ApJ 428, 555
Trümper J., 1983, Adv. Space Res. 2, 241
Tsuru T.G., Awaki H., Koyama K., Ptak A., 1997, PASJ 49, 619
Tully R.B., 1988, Nearby Galaxies Catalog. Cambridge University Press, Cambridge
Tully R.B., Shaya E.J., Pierce M.J., 1992, ApJS 80, 479
Veilleux S., Cecil G., Bland-Hawthorn J., et al., 1994, ApJ 433, 48
Veilleux S., Cecil G., Bland-Hawthorn J., 1995, ApJ 445, 152
Vogler A., Pietsch W., 1996, A&A 311, 35
Vogler A., Pietsch W., 1997, A&A 319, 459
Vogler A., Pietsch W., Kahabka P., 1996, A&A 305, 74
Voges W., Gruber R., Paul J., et al., 1992, In: Guyenne T.D., Hunt J.J. (eds.) Proc. European ISY conference, ESA ISY-3, p. 223
Willams R.M., Chu Y.-H., 1994, ApJ 439, 132
Wilson A.S., Elvis M., Lawrence A., Bland-Hawthorn J., 1992, ApJ 391, L75
Zimmermann H.-U., Belloni T., Boese G., et al., 1992, In: Guyenne T.D., Hunt J.J. (eds.) Proc. European ISY conference, ESA ISY-3, p. 231
Zimmermann H.-U., et al., 1994, "EXSAS users guide", edition 4, MPE Report 257